AUTHOR(S):

Pillai, Abhishek L.; Nagao, Jun; Awane, Ryo; Kurose, Ryoichi

京都大学学術情報リポジトリ
KURENAI 紅
Kyoto University Research Information Repository

Influences of liquid fuel atomization and flow rate fluctuations on spray combustion instabilities in a backward-facing step combustor

Abhishek L. Pillai*, Jun Nagao, Ryo Awane, Ryoichi Kurose

Department of Mechanical Engineering and Science, Kyoto University, Kyoto daigaku-Katsura, Nishikyo-ku, Kyoto 615-8540, Japan

ABSTRACT

Combustion instabilities occurring in spray combustion fields inside a backward facing step combustor have been investigated by performing large-eddy simulations (LES). In this study, the influence of fluctuations in the incoming oxidizer air velocity (caused by drastic pressure oscillations in the combustor during combustion instability) on the droplet diameter distribution (due to atomization) of the injected liquid fuel spray, as well as the influence of pressure oscillations on the fuel flow rate have been taken into consideration using appropriate models. For the temporal fluctuations in fuel droplet diameter distribution, a model for the Sauter Mean Diamter (SMD) of atomized droplets, obtained as a function of spray injection parameters and gas/liquid properties, is incorporated in the LES. Additionally, to consider the temporal fluctuations in fuel flow rate along with its phase difference with the pressure oscillations, a model derived from Bernoullis principle is proposed and employed in the LES. The objective is to examine in detail, the impacts of the fluctuations in fuel droplet diameter distribution and the fluctuations in fuel injection rate individually, as well as the impact of the mutual interaction of these two fluctuations, on the spray combustion instability characteristics. Results of the LES reveal that the temporal fluctuations in fuel droplet diameter distribution resulting from combustion instability, lead to a reduction in the intensity of pressure oscillations and hence the combustion instability's strength. Additionally, the temporal fluctuations in liquid fuel flow rate strongly influence the intensity of spray combustion instability, and it is observed that the combustion instability intensity increases with the increase in phase difference between the fuel flow rate fluctuations and pressure oscillations. Furthermore, the effect of the temporal fluctuations in fuel droplet diameter distribution resulting in the reduction of combustion instability intensity, becomes more pronounced as the phase shift between the fuel flow rate fluctuations and pressure oscillations becomes larger. It is clarified that the above-mentioned behavior of spray combustion instability, results from the change in the correlation between heat release rate fluctuations and pressure oscillations near the combustor's dump plane, which is caused by the change in the local residence time of fuel droplets and the local fuel droplet evaporation rate.

1. Introduction

The global civil air traffic has grown steadily over the last decade, and the demand for passenger and cargo transportation is expected to increase even further in the near future. This is evidenced by the International Civil Aviation Organization's (ICAO) annual global statistics [1], according to which 4.1 billion passengers were carried on scheduled services in 2017 alone (a 7.2% rise than its predecessor year). Therefore, the need for clean and environmentally friendly gas turbine engines with better combustion effi-

ciency has become ever so important. In particular, the regulations on toxic nitrogen oxide (NOx) emissions are becoming increasingly stringent, making the development of gas turbine engines that produce low levels of NOx highly desirable and mandatory [1]. Methods such as spraying fuel as a fine mist, pre-mixing air and fuel, and lean premixed prevaporized (LPP) combustion have attracted attention [2] as NOx regulatory compliance measures. Although the reduced combustion temperature of LPP combustion has the advantages of lower emissions of NOx and soot, this type of combustion also has increased unsteadiness, which increases the risk of occurrence of combustion instability [3–5].

Combustion instability is a form of unstable combustion generated inside the combustors of gas turbine engines, and is a

* Corresponding author.
E-mail address: pillai.abhisheklakshman.2e@kyoto-u.ac.jp (A.L. Pillai).

primary cause of combustor damage [4,5] and loud combustion noise. Hence, accurate prediction and control of this phenomenon is crucial for designing and developing efficient next generation engines. High amplitude pressure oscillations at discrete frequencies occur inside a combustor during such unstable combustion. Theoretically, combustion instability increases when there is a significant correlation between the heat release rate fluctuations and the pressure oscillations, i.e., the phase difference between the two fluctuations is small [6], because the energy of acoustic waves propagating in a combustor is increased as a consequence of the unsteady heat release (which means the pressure oscillations are amplified). However, the conditions leading to such an occurrence, its amplitude characteristics, and detailed mechanism are yet to be elucidated in depth. Currently, many studies are being conducted worldwide to clarify the mechanism of combustion instability and for its accurate prediction [e.g., [5],[7–11], [12]. In particular, compared to turbulent gaseous combustion with fuels such as natural gas, the combustion instability arising in spray combustion fields using liquid fuels such as kerosene, exhibits a more sophisticated phenomenon in which the dispersion and evaporation of liquid fuel droplets, and mixing of the evaporated fuel with the oxidizer followed by chemical reaction occur simultaneously and interactively, making the underlying physics very difficult to elucidate. In previous experimental studies, Lee et al. [9] determined that combustion instabilities can be actively controlled by modifying the properties of liquid fuel spray. Moreover, García et al. [10] reported that the evaporation of liquid fuel affects the frequency of combustion instability generated. However, because the data that can be collected from experiments are limited, the various factors affecting combustion instability characteristics have yet to be comprehensively clarified.

However, the remarkable improvement in computer performance and development of schemes/solvers capable of accurately and stably capturing the pressure perturbations in a combustion field in recent years, has allowed numerical analysis which can provide an abundance of data, to be used in studies on combustion instabilities [11–15]. Tachibana et al. [11], applied large-eddy simulation (LES) to the turbulent spray combustion field inside a liquid-fuel aero-engine combustor, and were the first to successfully reproduce combustion instability in a spray combustion field, as observed in their experiment performed at the Japan Aerospace Exploration Agency (JAXA). Later, Kitano et al. [12] performed LESs of turbulent spray combustion fields in a back-step flow combustor, to investigate the effect of initial droplet diameter of the liquid fuel spray injected into the combustor, on the combustion instability characteristics. It was clarified that the intensity of pressure oscillations during combustion instability is strongly affected by the initial fuel droplet diameter (the average droplet diameter d_{avg} for a fixed size distribution). However, they did not take into consideration the influence of temporal fluctuations in the fuel droplet size distribution and fuel flow rate on combustion instability. During combustion instability inside a back-step flow combustor, the velocity of incoming air fluctuates due to the pressure oscillations, which causes the fuel droplet size distribution to fluctuate as well (effect of varying level of atomization). Furthermore, the pressure oscillations also lead to fluctuations in the fuel flow rate.

Therefore, the purpose of this study is to elucidate the effects of temporal fluctuations in the droplet diameter distribution and the flow rate of liquid fuel into the combustor, on the spray combustion instability characteristics. In particular, a model capable of accounting for the temporal fluctuations in droplet diameter distribution of the injected fuel, due to secondary atomization of the liquid fuel is employed, and a model to account for the temporal fluctuations in fuel injection rate is proposed. By applying LES in-

corporating these models to the turbulent spray combustion fields in a back-step flow combustor, the effects of the individual models as well as the effects of their mutual interaction, on the characteristics of combustion instability can be investigated in detail.

2. Large-eddy simulation

Combustion instability is a transient phenomenon in which turbulent flow, combustion reaction and acoustic resonance are intertwined in a complex manner. Therefore, in order to realize its precise prediction, it is necessary to perform computations in a large domain that includes not only the targeted combustor region, but also the sections upstream and downstream of the combustor. Moreover, the computational grid must be sufficiently fine in the regions where combustion reaction occurs, and the simulation must be performed over a long time period to acquire time series data for analyzing the oscillation frequency. Hence, Large-eddy Simulation (LES) is adopted as the computation strategy for this work. The effect of liquid fuel atomization on combustion instability characteristics is investigated in detail, for turbulent spray combustion field in a back-step flow combustor. Additionally, the influence of temporal fluctuations in liquid fuel mass flow rate due to pressure fluctuations inside the combustor (arising from combustion instability itself) on the combustion instability characteristics are also examined. Furthermore, the influence on combustion instability characteristics is examined when phase differences are applied to the temporal fluctuations of the liquid fuel mass flow rate.

2.1. Governing equations

For LES of the gas-phase, which is treated as an Eulerian continuum, the Favre-filtered form of the conservation equations of mass, momentum, energy and mass fraction of chemical species are solved along with the state equation for ideal gas. Details of these governing equations can be found in the previous work [12]. For evaluation of the unresolved subgrid-scale (SGS) terms, the dynamic Smagorinsky model [16,17] is employed, and the spatial filter function used in the LES is a Gaussian filter. In order to resolve the flame-front on the computational grid of the LES [18–22] by artificially thickening it, the flame thickening factor F defined below, is introduced in the Favre-filtered conservation equations of enthalpy and species mass fraction [12]

$$F = (F_{max} - 1)\Omega + 1. \tag{1}$$

where the maximum flame thickening coefficient is $F_{max} = 12$. The term Ω in the above equation is called the flame sensor [18,21,22] which is used to detect the flame-front position. Ω varies from zero in fully burnt or unburnt regions to unity inside the reaction zone and is defined as

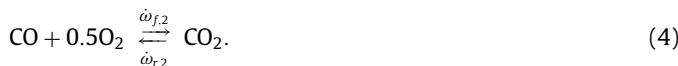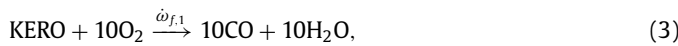$$\Omega = \tanh\left(\alpha \frac{q}{q_{max}}\right). \tag{2}$$

where, q is the local heat release rate, and q_{max} is the maximum heat release rate computed from a one-dimensional laminar flame simulation. The thickness of the transition layer between non-reacting and reacting zones is regulated by the parameter α, and in the present simulations $\alpha = 5$ is used [12]. Thus, the dynamic version of Thickened Flame Model (TFM) is applied which smoothly modulates the thickening factor F from unity in the regions away from the flame front to large values inside the flame. Thickening is applied only in the vicinity of the reaction zones, and fuel droplet evaporation is active in the regions away from the flame front as well. As described later in Fig. 8, high rates of fuel droplet evaporation occur mainly in regions away from or outside the reaction zones. Hence, it is assumed that the influence of dynamically TFM

on fuel droplet evaporation is small enough to warrant any corrections for heat and mass exchanges between the dispersed- and gas-phases in the present LESs. Artificial thickening of the flame-front suppresses its interaction with the SGS turbulence, therefore, an efficiency function E is also introduced in the transport equations of enthalpy and species mass fraction [12], which serves as a correction for the loss of flame surface wrinkling due to artificial flame thickening, and is computed using the procedure described in [19,21].

Evolution of the fuel spray is governed by a set of Lagrangian equations describing the dynamics of individual fuel droplets which are treated as point masses. These are the governing equations for droplet trajectory $\boldsymbol{x}_d$, velocity $\boldsymbol{u}_d$, temperature T_d, and mass m_d, whose details can be found in previous works [12,23,24]. A non-equilibrium Langmuir-Knudsen model [25–27] is employed for droplet evaporation. Source terms appearing in the governing equations of the gas-phase, which represent the interactions between dispersed-phase (fuel droplets) and gas-phase [12] are calculated using the Particle-Source-In-Cell (PSI-Cell) approach [28], thereby realizing two-way coupling. Detailed calculation procedures of these source terms and the dispersed-phase are described in [23,24,29], and are not repeated here for the sake of brevity.

2.2. Reaction model

Fuel for the liquid spray considered in this work is kerosene (hereafter referred to as KERO), originally composed of $C_{10}H_{22}$ (76.7 wt%), C_9H_{12} (13.2 wt%) and C_9H_{18} (10.1 wt%). However, KERO is assumed to be an equivalent single species ($C_{9.7396}H_{20.0542}$) of these three species [30]. A two-step reduced chemical scheme proposed by Franzelli et al. [30] is used to model the combustion of gaseous KERO. The reduced chemical scheme takes into account six species (KERO, O_2, H_2O, CO_2, CO and N_2) and the following two reactions.

$$KERO + 10O_2 \xrightarrow{\dot{\omega}_{f,1}} 10CO + 10H_2O, \tag{3}$$

$$CO + 0.5O_2 \underset{\dot{\omega}_{r,2}}{\overset{\dot{\omega}_{f,2}}{\rightleftharpoons}} CO_2. \tag{4}$$

Where, $\dot{\omega}_{f,1}$ is the forward reaction rate for the oxidation of KERO in Eq. (3), and $\dot{\omega}_{f,2}$ and $\dot{\omega}_{r,2}$ are the forward and reverse reaction rates, respectively for the reversible CO oxidation reaction in Eq. (4). Calculation procedure for the reaction rates $\dot{\omega}_{f,1}$, $\dot{\omega}_{f,2}$ and $\dot{\omega}_{r,2}$ are described in [30,31]. The local equivalence ratio required to calculate these reaction rates are estimated using the standard Bilger's definition, and its calculation method is the same as that detailed in a previous work [32]. Furthermore, to estimate the reaction rates $\dot{\omega}_{f,1}$, $\dot{\omega}_{f,2}$ and $\dot{\omega}_{r,2}$ in a given computational cell, the temperature and the molar concentration of species corresponding to that computational cell are used [30–32]. This reaction model is capable of accurately reproducing important combustion quantities, such as laminar flame speed, adiabatic flame temperature, equilibrium CO levels, and ignition delays for a wide range of equivalence ratio, fresh gas temperature and pressure [30]. Moreover, it has also been validated for the accurate prediction of flame propagation characteristics of fuel droplet arrays [31].

2.3. Atomization model

One of the objectives of the present study is to analyze the influence of combustion instability on the atomization (diameter distribution) of liquid fuel spray being injected into the back-step combustor. Recently, Lee et al. [33] used the integral from of the
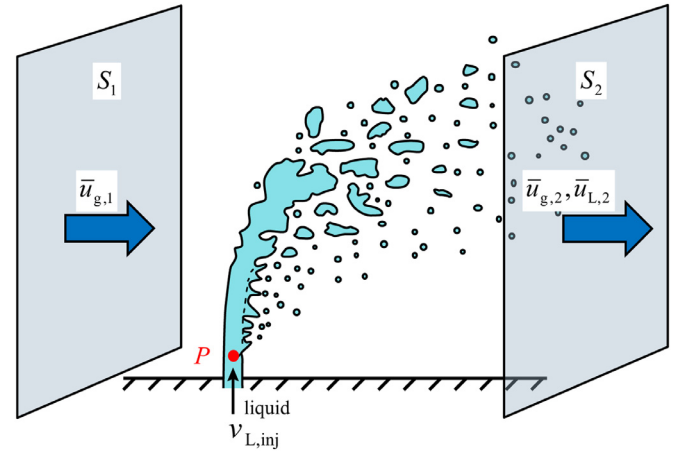

Fig. 1. Schematic of liquid jet atomization in crossflow. (For interpretation of the references to color in this figure legend, the reader is referred to the web version of this article.)

conservation equations of mass, momentum and energy to theoretically derive a cubic relation for the droplets' Sauter Mean Diameter (SMD) post-atomization, for liquid sprays in cross-flows. Hence, this approach does not involve any ad-hoc modeling or unphysical descriptions of the atomization process [33]. Moreover, this model has been extensively validated against experimental data for spray atomization in cross-flow configuration [33], which makes it suitable for application in the present study where fuel spray is injected into air cross-flow (described later in Section 2.5). The expression for calculating the SMD (referred to as Lee model or SMD modulation hereafter) of injected fuel droplets, which relates the SMD to a cubic function of gas-phase velocity ratio is given by

$$SMD = \frac{3\sigma + \sqrt{9\sigma^2 + \frac{K\mu_L \bar{u}_{L,2}^2}{\bar{v}_{L,inj}A_{inj}}\left(\frac{\rho_L}{2}\left(\bar{v}_{L,inj}^2 - \bar{u}_{L,2}^2\right) + \frac{A_c}{\bar{v}_{L,inj}A_{inj}}\frac{\rho_{g,1}}{2}\left(\bar{u}_{g,1}^3 - \bar{u}_{g,2}^3\right)\right)}}{\left(\frac{\rho_L}{2}\left(\bar{v}_{L,inj}^2 - \bar{u}_{L,2}^2\right) + \frac{A_c}{\bar{v}_{L,inj}A_{inj}}\frac{\rho_{g,1}}{2}\left(\bar{u}_{g,1}^3 - \bar{u}_{g,2}^3\right)\right)}, \tag{5}$$

$$Ac = \left[3.44d_{inj}\sqrt{\frac{\rho_L \bar{v}_{L,inj}^2}{\rho_{g,1}\bar{u}_E Sg, 1^2}}\right]$$

$$\times \left[7.86d_{inj}\left(\frac{\rho_L \bar{v}_{L,inj}^2}{\rho_{g,1}\bar{u}_{g,1}^2}\right)^{0.17} \times 8.06^{0.33}\right], K = 0.112. \tag{6}$$

here, $\rho_{g,1}$ and $\bar{u}_{g,1}$ are the cross-sectional plane averaged gas-phase density and velocity, respectively, upstream of the fuel injection point (cross-section S_1 in Fig. 1). $\bar{u}_{g,2}$ is the downstream cross-sectional plane (S_2 in Fig. 1) averaged gas-phase velocity, $\bar{v}_{L,inj}$ is the injection velocity of fuel droplets, and $\bar{u}_{L,2}$ is the mean velocity of fuel droplets after secondary atomization. The schematic in Fig. 1 also illustrates these quantities. Furthermore, σ represents the surface tension of liquid fuel, ρ_L is the liquid fuel density, μ_L is the dynamic viscosity of liquid fuel, A_{inj} is the injector exit area, d_{inj} is the injector exit diameter, A_c is the cross-sectional area of the spray given by Eq. (6), and K is a proportionality constant for the viscous dissipation term which is the only adjustment parameter in this model, and is determined based on the flow velocity and the value of SMD. Figure 2 shows the variation of SMD of liquid fuel droplets with the cross-sectional plane averaged air velocity $\bar{u}_{g,1}$, calculated using the Lee model. It can be seen that as the inflow air velocity increases, the resulting droplet size (SMD) decreases and vice-versa. When combustion instability occurs, the resulting pressure fluctuations inside the combustor cause the incoming air flow velocity to fluctuate accordingly, which in
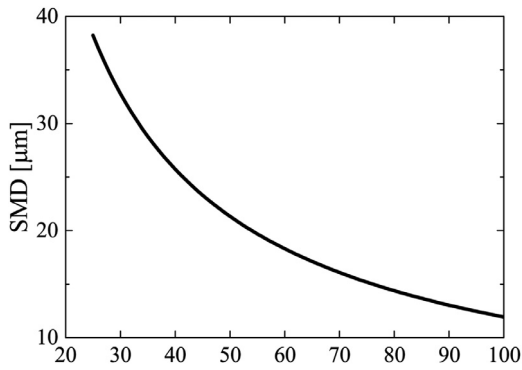
Fig. 2. Effect of incoming air-velocity $u_{g,1}$ on SMD using Lee model [33].
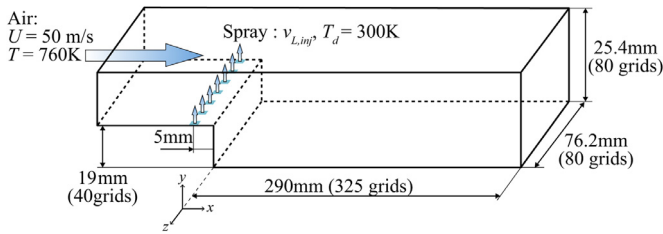

Fig. 3. Computational domain and conditions.

turn produces fluctuations in the SMD of fuel droplets as a consequence of the varying degree of atomization. In the present simulations, the SMD computed using Eq. (5) with instantaneous gas- and liquid-phase injection parameters and properties, is used to calculate the size distribution of fuel droplets to be injected (described in Section 2.5). So, with this atomization model, it is assumed that the spray is already established at the fuel injection positions, meaning the atomization process is assumed to be instantaneous and this is a limitation of the Lee/atomization model. However, such an assumption is reasonable in the context of the present LESs, since combustion starts occurring after the backward-facing step downstream of the fuel injection positions (as will be evident later from Figs. 7 and 8 and their accompanying discussion in Section 3.1). Furthermore, the computational cost of modeling primary atomization is still quite prohibitive, hence, the Lee model has been chosen for this study.

2.4. Variable Mass Flow Rate model (VMFR model)

The influence of pressure fluctuations inside the back-step combustor (caused by combustion instability) on the incoming air flow, and the injected fuel spray is also considered in this study. In the LESs, incoming air in the combustor has a sufficiently large inflow area (see Fig. 3), hence, its velocity fluctuations adjust automatically to the pressure fluctuations. On the other hand, fluctuations in the injection velocity of the liquid fuel spray which is an incompressible fluid, are considered using the following Variable Mass Flow Rate model (hereafter referred to as VMFR model), that can be derived from the Bernoulli's equation.

$$\bar{v}_{L,inj} = \begin{cases} \bar{v}_{ave} \times \sqrt{\dfrac{P_0 - P\left(t_{now} - T\frac{\phi_{ph}}{2\pi}\right)}{P_0 - P_{ave}}}, & for \quad P_0 > P\left(t_{now} - T\frac{\phi_{ph}}{2\pi}\right) \\ \bar{v}_{min}, & for \quad P_0 \leq P\left(t_{now} - T\frac{\phi_{ph}}{2\pi}\right) \end{cases}$$

(7)

Here $\bar{v}_{L,inj}$ is the instantaneous fuel injection velocity, $\bar{v}_{ave}$ is the mean fuel injection velocity ($\bar{v}_{ave} = 2$ m/s), P_{ave} is the time averaged pressure at the fuel injection position (represented by point

P in red color in Fig. 1, just above the fuel injection port exit), T is the period of pressure oscillation, t_{now} is the current time, $P(t)$ is the transient pressure just above the fuel injection position's exit (point P in Fig. 1 at the injection port exit) at time instance t, ϕ_{ph} is the phase difference between fuel flow rate fluctuations and pressure oscillations, and P_0 is the fuel injection pressure expressed as the summation of pump pressure P_{pump} and P_{ave}. In Eq. (7) above, it is assumed that when the instantaneous value of pressure at the fuel injection position $P(t_{now} - T\frac{\phi_{ph}}{2\pi})$ becomes greater than or equal to P_0, $\bar{v}_{L,inj}$ is equal to a small value $\bar{v}_{min}$ (10% of $\bar{v}_{ave}$). Ideally, the fuel injection should be cut-off when the transient pressure $P(t)$ exceeds the fuel injection pressure P_0. However, in the initial test runs for the various cases in which VMFR model is applied, it was observed that if the fuel injection velocity $\bar{v}_{L,inj}$ is made zero for the duration when $P(t_{now} - T\frac{\phi_{ph}}{2\pi})$ exceeds P_0, the overall equivalence ratio computed using the fuel and air mass flow rates over the time period of one oscillation cycle could not be maintained at 1.0. Hence, some initial trial runs of the simulations were conducted to optimize the value of $\bar{v}_{min}$, and it was found that $\bar{v}_{min} = 10\%$ of $\bar{v}_{ave}$ worked well to maintain the overall equivalence ratio close to 1.0 in all cases. The pump pressure P_{pump} is obtained from Bernoulli's equation as

$$P_{pump} = \frac{1}{2}\rho_L \bar{v}_{ave}^2.$$

(8)

It has been confirmed in a previous experimental investigation conducted by Ghoniem et al. [34] that when combustion instability occurs, the velocity fluctuations of incoming air are 90° out of phase with the pressure fluctuations. Moreover, one can also expect fluctuations in the liquid fuel spray's flow rate, since it is susceptible to the pressure fluctuations inside the combustor. However, it is difficult to accurately measure the liquid fuel flow rate fluctuations due to limitations of measuring equipment. Additionally, many experimental studies have been carried out to suppress combustion instabilities in spray combustion fields by actively controlling the fuel injection rate [e.g., [9],[35,36],[37]. Most of the previous studies analyze the fluctuations in pressure, velocity and heat release rate, but rarely investigate the influences of spatial distributions of liquid fuel droplets, evaporation rate, fuel, and their temporal variations on combustion instability. Furthermore, studies using numerical simulations to explore the aforementioned physical parameters are also scarce to the best of the authors' knowledge. Therefore, in addition to considering fluctuations in the flow rate of liquid fuel spray due to combustion instability in the present study, the active control of liquid fuel injection rate is also considered via. the phase difference ϕ_{ph}, and LESs of various cases are performed with different values of ϕ_{ph}, to investigate the impact of temporal variations of fuel injection rate on combustion instability.

2.5. Computation details and calculation conditions

The computational domain of the combustor section is shown in Fig. 3, while the entire computational domain is illustrated in Fig. 4. The computational domain-size and the conditions are set in accordance with the previous study by Kitano et al. [12], except for the combustor length l and the injection velocity of liquid fuel $\bar{v}_{L,inj}$. The combustor length has been increased from $l = 200$ mm in the previous study [12] for spray combustion simulations to $l = 290$ mm in the present study. The reason for increasing the combustor length in this study is the modification made to the fuel injection configuration. In the LESs performed by Kitano et al. [12], fuel droplets were injected 5 mm upstream of the back-step similar to the present LESs, however, they were injected along a continuous slit (see Fig. 12 in [12]). In the present configuration, fuel droplets are injected from 7 injection ports arranged
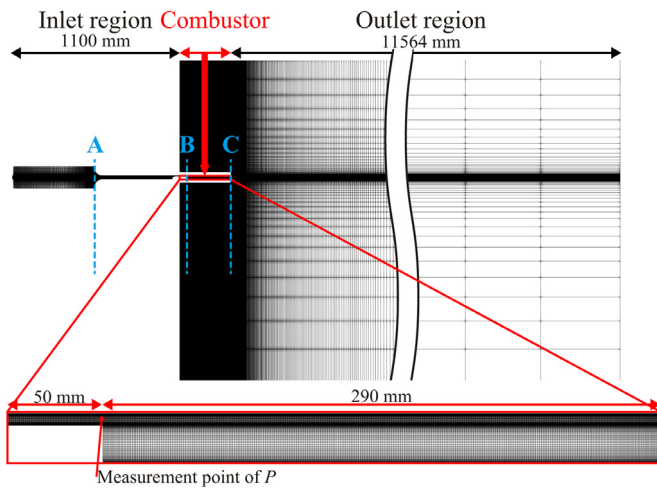
Fig. 4. Computational grid.

Fig. 5. Effect of air-velocity $\overline{u}_{g,1}$ on injected fuel droplet size distribution.

Table 1
Cases investigated in this study ($\times$: Model is not applied, $\bigcirc$: Model is applied). ϕ_{ph} is the phase shift angle by which the fuel mass flow rate fluctuations lag the combustor pressure oscillations.

Case	Lee model (SMD modulation)	VMFR model	Phase shift angle ϕ_{ph}
NA-1	$\times$	$\times$	-
NA-2	$\times$	$\bigcirc$	0°
NA-3	$\times$	$\bigcirc$	90°
NA-4	$\times$	$\bigcirc$	180°
NA-5	$\times$	$\bigcirc$	270°
A-1	$\bigcirc$	$\times$	-
A-2	$\bigcirc$	$\bigcirc$	0°
A-3	$\bigcirc$	$\bigcirc$	90°
A-4	$\bigcirc$	$\bigcirc$	180°
A-5	$\bigcirc$	$\bigcirc$	270°

at equal intervals as depicted in Fig. 3. Initial test run with this fuel injection configuration and the same combustor length as the previous study [12] yielded very weak nonlinear limit cycle oscillation/combustion instability. This was caused by the alteration of heat release rate topology due to change in the fuel injection configuration, and a consequent weakening of the phase relationship/coupling between heat release rate fluctuations and pressure oscillations. The combustor length was then gradually increased in the test runs until a strong enough combustion instability occurred for a combustor length of $l = 290$ mm.

The computational geometry used in this study as well as that of Kitano et al. [12] is similar to the experimental test rig of Smith and Zukoski [38]. In Fig. 4, the section up to location A from the left end of the inlet region is the plenum chamber. The left end of the plenum chamber has a small inlet area through which air supply enters into the domain. Incoming air temperature is $T_{in} = 760$ K and the mass flow rate of incoming air $\dot{m}_{air}$ is kept constant. At the inlet boundary, Neumann condition is applied for the inlet pressure P_{in} and inlet density ρ_{in} is calculated using ideal gas law as $\rho_{in} = P_{in}/RT_{in}$. Incoming air velocity at the inlet boundary u_{in} fluctuates in accordance with the fluctuations of P_{in}. The air mass flow rate can be expressed as $\dot{m}_{air} = \rho_{in}A_{in}u_{in}$, where A_{in} is the inlet area. Using the ideal gas equation, the air mass flow rate equation can be recast as follows to yield the solution for u_{in}.

$$u_{in} = \frac{\dot{m}_{air}}{\rho_{in}A_{in}} = \frac{\dot{m}_{air}RT_{in}}{A_{in}P_{in}} \qquad (9)$$

Since $\dot{m}_{air}$, R, T_{in} and A_{in} are constant values, u_{in} varies depending on the variation of P_{in} as per the above equation. No-slip boundary condition is applied at the wall surfaces, and the walls are assumed to be isothermal with their temperature fixed at 760 K. The x, y, and z axes correspond to the main channel/flow direction, vertical direction, and span direction, respectively (as shown in Fig. 3), and the step's streamwise position is set to $x = 0$ mm. Air is introduced into the combustor through the inflow section, and fuel droplets (KERO) are injected vertically upwards with velocity $\overline{v}_{L,inj}$ from the position 5 mm upstream of the step. The injection rate of fuel droplets is adjusted such that, the overall equivalence ratio is 1.0 over the time period of one oscillation cycle (as explained in Section 2.4), and the initial temperature of fuel droplets is 300 K. Figure 2 shows an example of the change in SMD of injected fuel droplets with respect to the cross-sectional plane averaged air velocity $\overline{u}_{g,1}$. The probability density function (PDF) for droplet diameter distribution of the liquid fuel is defined using a modified Nukiyama-Tanasawa function [39]. Figure 5 shows the
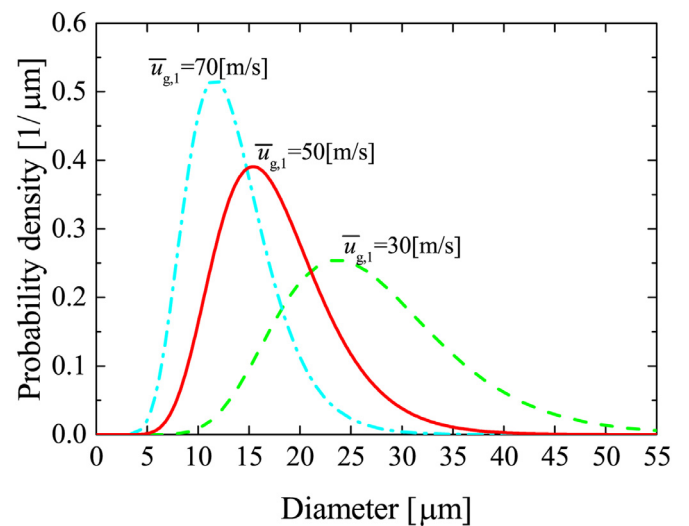
droplet size distributions of liquid fuel spray at the time of injection, corresponding to various values of the cross-sectional plane averaged air velocity $\overline{u}_{g,1}$. The SMDs required to compute these droplet size distributions (since, the modified Nukiyama-Tanasawa function [39] uses SMD as a parameter) that vary in time depending on the value of $\overline{u}_{g,1}$, are obtained using the Lee model [Eq. (5)]. As $\overline{u}_{g,1}$ increases, the SMD decreases, and the droplet size distribution gets biased towards smaller size and vice versa. The droplet diameter distribution of the injected fuel spray for cases without the Lee model, i.e., Cases NA-1 to NA-5 (summarized in Table 1 and explained below) in which SMD modulation is not applied, is based on the measured droplet diameter distribution of a previous experiment conducted by Moriai et al. [40] for a real gas turbine combustor. Fitting parameters of the modified Nukiyama-Tanasawa distribution function are calculated so as to obtain a best fit curve to this measured droplet diameter distribution. The average droplet diameter d_{avg} corresponding to this droplet size distribution is 18 μm and the corresponding SMD is 22.5 μm. The reason for choosing this droplet size distribution with $d_{avg} = 18$ μm is that, in the previous study by Kitano et al. [12], the influence of d_{avg} of injected fuel spray on the strength of combustion instability (intensity of pressure oscillations) was investigated, and it was found that combustion instability was strongest for a specific value of d_{avg}, and that d_{avg} corresponded to this exact droplet size distribution based on Moriai et al.'s measurements [40] (with $d_{avg} = 18$ μm).

Table 1 summarizes the cases that have been examined and compared in this study. First, in Section 3.1, Case NA-1 and Case A-1 are examined and compared, and the influence of fluctuations

in initial droplet size distribution of liquid fuel on the combustion instability characteristics is investigated. Next, in Section 3.2, Cases NA-2 to NA-5 (i.e., cases without the Lee model) are compared and examined to investigate the effect of fluctuations of liquid fuel flow rate (along with the phase difference ϕ_{ph} applied in the VMFR model) on the combustion instability characteristics. In Cases NA-1 to NA-5, the atomization/Lee model is not applied and a presumed droplet size distribution with SMD = 22.5 μm as explained above is imposed. Hence, Cases NA-1 to NA-5 are referred to as cases "without SMD modulation" or cases "without Lee model" for the remainder of this article. Finally, in Section 3.3, the cases with Lee model (or cases with SMD modulation), i.e., Cases A-2 to A-5 are examined and compared against the cases without Lee model (i.e., Cases NA-2 to NA-5), in order to investigate the influence of temporal fluctuations of both the droplet size distribution and the liquid fuel flow rate, and their interaction on the combustion instability characteristics. The phase difference ϕ_{ph} applied between the temporal fluctuations of liquid fuel flow rate and the pressure oscillations in each case, is set as shown in Table 1.

The LESs of all the spray combustion cases listed in Table 1 are performed using an in-house thermal flow analysis code FK^3 [12,24,29,31,41–47]. This code's solver employs a pressure-based semi-implicit (fractional-step) algorithm for compressible flows [48]. The computational domain is discretized using a non-uniform staggered Cartesian grid, with fine grid-spacing near the walls. There are approximately 2.4 million grid points in the combustor section, and the total number of grid points in the whole computational domain including the outflow is about 21.5 million. The spatial derivatives in the governing equations of the gas-phase are approximated using a second-order accurate central difference scheme, except for the convection terms in the governing equations of the gas-phase enthalpy and chemical species mass fractions which are evaluated using the WENO scheme [49]. The third-order explicit TVD Runge-Kutta scheme is used for time integration of the convection terms. All thermodynamic properties and transport coefficients are calculated according to CHEMKIN [50,51] taking temperature dependence into account. The validity of the present LES for predicting the combustion instabilities has been confirmed by comparison with an experiment [38] for gas combustion instability in the previous work by Kitano et al. [12]. The in-house code FK^3 has also been successfully applied for simulating spray combustion problems in the past and also validated [52]. The CPU time required per case of this computation is approximately 480,000 h (about 470 h of real time) by parallel computation using 1024 cores on a SGI:ICE X supercomputer (with Intel Xeon E5-2670 processor) at the Central Research Institute of Electric Power Industry (CRIEPI), Japan.
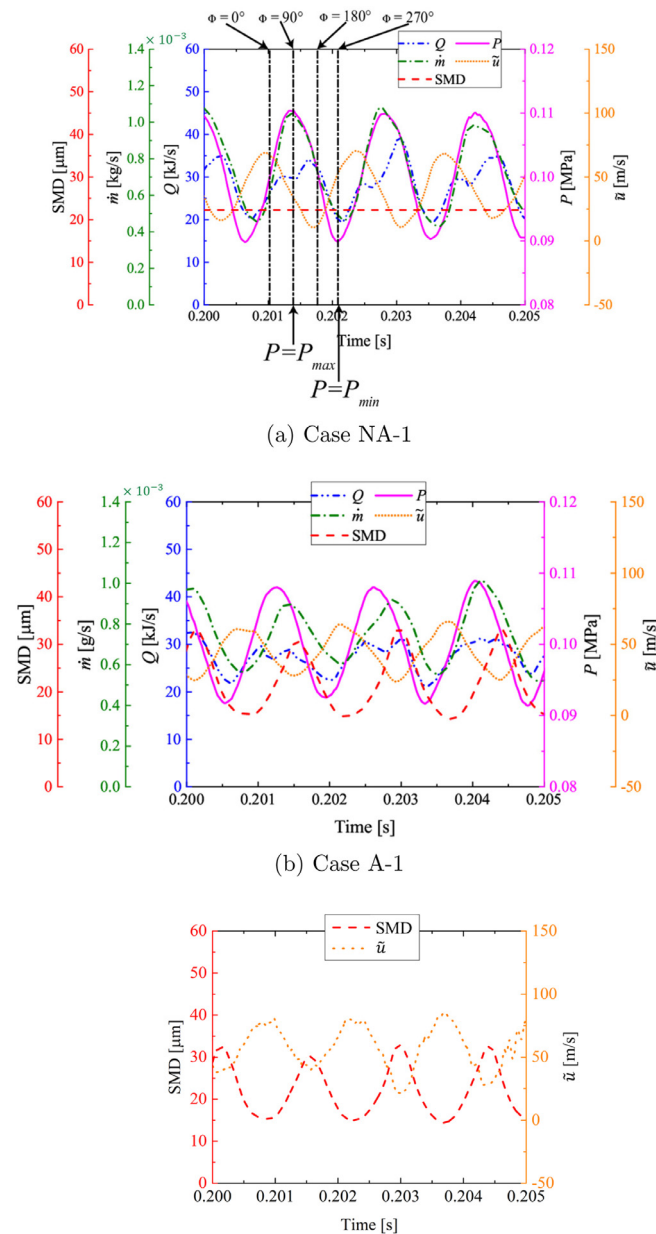
3. Results and discussion

3.1. Influence of time variations of liquid fuel droplet diameter distribution on combustion instability

First, Case NA-1 (without SMD modulation) and Case A-1 (with SMD modulation) are considered, and the occurrence of combustion instability in these Cases is confirmed. Figure 6 shows the time variations of pressure P, heat release rate Q, streamwise velocity $\tilde{u}$, fuel droplet evaporation rate $\dot{m}$, and SMD of injected fuel droplets, in Case NA-1 and Case A-1. Here, P represents the value of pressure measured at a point on the dump plane (i.e., the interface between the combustor and inlet duct) as shown in Fig. 4, $\tilde{u}$ represents the cross-sectional ($y - z$ plane)-averaged value of the streamwise velocity at the dump plane, Q and $\dot{m}$ represent the total values of heat release rate and fuel droplet evaporation rate, respectively, inside the combustor, and SMD represents the value

computed using the Lee model in Eq. (5) (note that the SMD is constant in Case NA-1, since the atomization/Lee model is not applied and the injected droplet size distribution does not vary in time). The inspection cross-section for $\tilde{u}$ used in the Lee model to compute $\bar{u}_{g,1}$ (see Fig. 1), is located 8 mm upstream of the fuel injection ports. Ideally the inspection cross-section for computing $\bar{u}_{g,1}$ should be placed close to the fuel injection ports' position, to get an accurate estimate of the incoming air's kinetic energy. However, when combustion instability occurs, the pressure oscillations induce fluctuations in the velocity of incoming air/gas-phase which in turn induces fluctuations in the velocity of injected fuel droplets. As a result of the pressure oscillations, some droplets are pushed backwards and get displaced upstream of the fuel injection ports. Therefore, the rationale for placing the inspection cross-section for computing $\bar{u}_{g,1}$ 8 mm upstream of the fuel injection ports, is to ensure that no fuel droplets cross or are present at this cross-section, otherwise the estimate for $\bar{u}_{g,1}$ will not be correct, since it will include the effect of momentum exchange between the gas- and dispersed-phases.

The phase ϕ shown in Fig. 6(a) is defined using the time variation of pressure P as a reference. $\phi = 0°$ is defined as the instance when P reaches atmospheric pressure value P_{atm} as it increases during its oscillations, $\phi = 90°$ is defined as the instance when P reaches its maximum value P_{max}, $\phi = 180°$ is defined as the instance when P reaches the atmospheric pressure P_{atm} as it decreases during its oscillations, and $\phi = 270°$ is defined as the instance when P reaches its minimum value P_{min}. The figure shows that the various physical quantities oscillate with a period that is approximately constant in both Case NA-1 and Case A-1. It can be seen that the phase difference between the variations of P and $\tilde{u}$ is approximately 90°. This phase difference was also observed in a previous experiment [34], and is caused by classical air column vibration mechanism (where fluid acceleration is governed by the pressure gradient). Moreover, in Case A-1, the SMD varies in time and corresponds to the fluctuations of $\tilde{u}$. This is apparent from Fig. 6(b) as well as Fig. 6(c). In Fig. 6(c), $\tilde{u}$ represents the streamwise air velocity computed 8 mm upstream of the fuel injection position (which is the inspection cross-section used for computing $\bar{u}_{g,1}$, required for the Lee/atomization model), and at the center of the inlet duct. The phase difference between the variations of SMD and $\tilde{u}$ in both Fig. 6(b) and (c) is 180°, and in accordance with the Lee model (SMD decreases with increasing air inflow velocity and vice-versa, see Fig. 2). Additionally, the phase of the variations of $\dot{m}$ lags that of $\tilde{u}$ by approximately 90° in Case NA-1, and 120° in Case A-1. The phase difference between $\dot{m}$ and $\tilde{u}$ depends on the distance from the fuel injection location to the combustion reaction region, the evaporation properties of the fuel, and the combustion properties.

To understand more about the flow-fields and the nature of the flames obtained from the LESs, instantaneous distributions of gas-phase temperature and Flame Index (*FI*), on the central $x - y$ plane of Case NA-1 are illustrated in Fig. 7, at various time instances/phases ranging from $\phi = 0° - 270°$. The left column shows the instantaneous distributions of gas-phase temperature along with the dispersed fuel droplets (represented by grey entities), while the right column shows the instantaneous distributions of *FI*. Here, the standard definition of *FI* is used, i.e. $FI = \nabla Y_F \cdot \nabla Y_O$, where Y_F and Y_O are the mass fractions of fuel and oxidiser, respectively. Furthermore, *FI* distributions shown in Fig. 7 have been weighted by the heat release rate, in order to avoid the influence of regions with pure droplet evaporation and pure mixing (i.e., regions without reactions). The instantaneous distributions of gas-phase temperature and fuel droplets indicate that, as the injected fuel droplets convect downstream with the flow, they disperse and evaporate. Subsequent combustion of the evaporated fuel occurs and flame is formed behind the back-step.

(a) Case NA-1

(b) Case A-1

(c) Time variations of SMD and incoming air's streamwise velocity $\widetilde{u}$ computed 8mm upstream of the fuel injection position at the center of the inlet duct for Case A-1.

Fig. 6. Comparisons of time variations of pressure P, heat release rate Q, streamwise velocity $\widetilde{u}$, droplet evaporation rate $\dot{m}$, and droplet Sauter Mean Diameter (SMD), between cases without (Case NA-1) and with (Case A-1) SMD modulation.

Droplet count reduces with increasing downstream distance from the dump plane as a consequence of evaporation and combustion. For Cases NA-1, the droplet relaxation time τ_d is in the range of $\tau_d = 5.53 \times 10^{-8} - 8.48 \times 10^{-4}$ s (depending upon the instantaneous droplet size and properties of the gas-phase surrounding it). The droplet relaxation time values presented this study, include the correction to Stokes drag for droplet motion and evaporation as explained in [24,27,29]. The turbulent time scale τ_t is approximately 7.44×10^{-3} s. Here, τ_t is defined as the ratio of the streamwise integral length scale value computed at the location 40 mm downstream of the back-step (at the center of the combustor's cross-section), to the standard deviation of gas-phase streamwise velocity at that location. Stokes number St, based on the above-defined droplet relaxation time τ_d and turbulent time scale τ_t

is thus, $St = \tau_d/\tau_t$ and is in the range of $7.42 \times 10^{-6} - 0.114$. Therefore, fuel droplets get entrained into the large vortical structures that are periodically generated behind the back-step (due to oscillations of $\widetilde{u}$), and this is more clearly visible in Fig. 7(a) and (b). Judging from the distributions of fuel droplets, gas-phase temperature and FI at different phases ϕ, it is evident that the dispersed droplet clusters and the gas-phase experience periodically pulsating motion due to the influence of combustion instability (i.e., pressure oscillations). As for the nature of flame generated, the distributions of FI shown in the right column of Fig. 7 at different phases ϕ are predominantly positive (although some small regions with negative FI do exist). This indicates that premixed combustion is dominant in Case NA-1, with the exception of some minor zones with non-premixed combustion. Similar tendencies
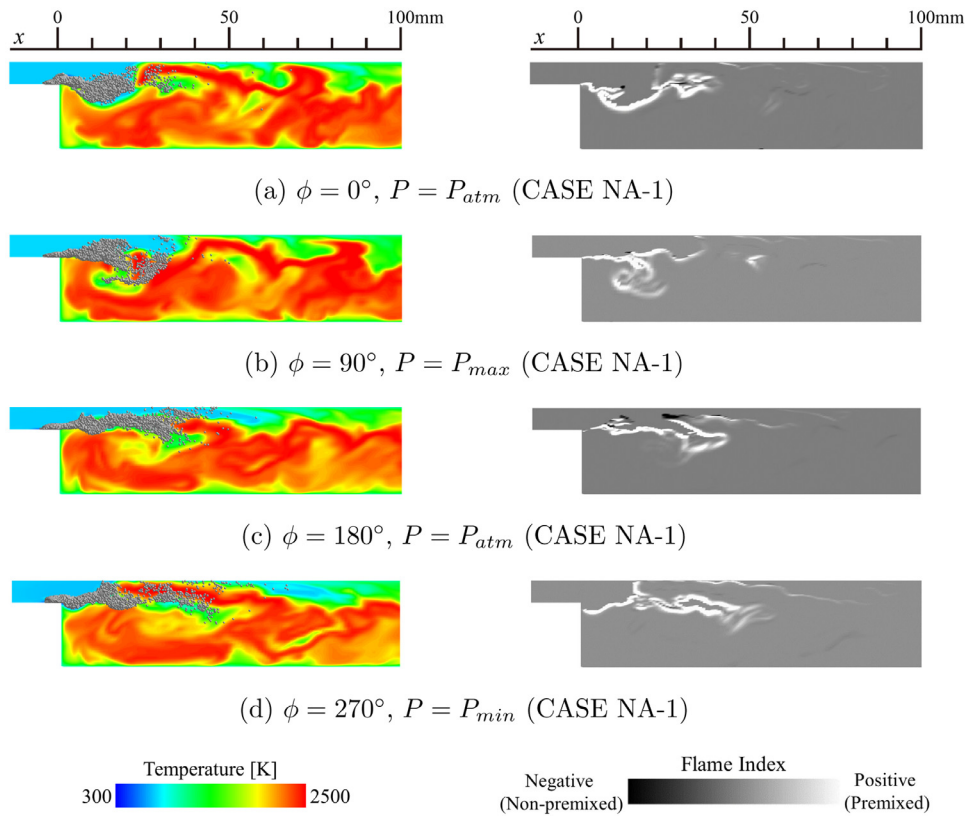
Fig. 7. Instantaneous distributions of gas-phase temperature along with dispersed fuel droplets (left column), and Flame Index (right column), on the central $x - y$ plane for Case NA-1 at different values of phase ϕ.
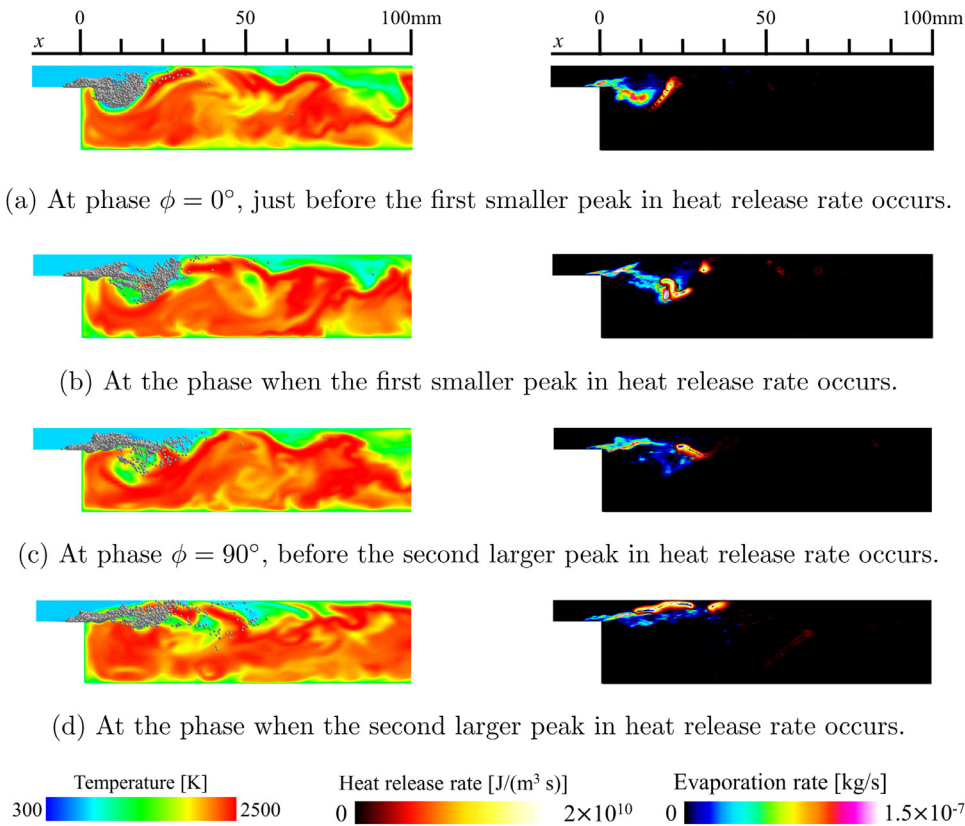

Fig. 8. Instantaneous distributions of gas-phase temperature along with dispersed fuel droplets (left column), and heat release rate and fuel droplet evaporation rate (right column), on the central $x - y$ plane for Case NA-1.

were observed for all the other cases investigated in this study, and hence their results are not shown for the sake of brevity.

Moreover, the temporal variations of total heat release rate Q inside the combustor, depicted in Fig. 6 have a double peak feature. The general trend observed in Fig. 6(a) for Case NA-1 is that, the first peak of Q (smaller in magnitude) occurs during the time period when pressure rises from P_{min} to P_{max} (i.e. during $\phi = 270° - 90°$), soon after the phase $\phi = 0°$ ($P = P_{atm}$), and the second peak of Q (larger in magnitude) occurs during the time period when pressure falls from P_{max} to P_{min} (i.e., during $\phi = 90° - 270°$), right before the phase $\phi = 180°$ ($P = P_{atm}$). To analyze the mechanism responsible for this double peak behavior of Q, Fig. 8 illustrates the instantaneous distributions of gas-phase temperature (along with fuel droplets) on the left column, and those of fuel droplet evaporation rate and heat release rate on the right column, for Case NA-1 at different phases/time instances. The temperature and fuel droplet distributions shown in Fig. 8(a) at the phase $\phi = 0°$, correspond to the instance when the streamwise velocity $\tilde{u}$ of incoming air is maximum, and the vortex shedding process is occurring. Consequently, during the period $\phi = 270° - 90°$, fuel droplets get entrained into this large vortex near the back-step, and they have sufficient residence time to evaporate. As a result, the evaporation rate in the vortex region becomes large, as shown in Fig. 8(a) (right) which subsequently leads to ignition of the fuel-air mixture, thereby causing an increase in the heat release rate (around $x \approx 25$ mm) as depicted in Fig. 8(b), which corresponds to the phase when the first smaller peak of Q occurs. After the first peak of Q occurs, the vortex that is periodically shed during $\phi = 270° - 90°$ is conveyed downstream as depicted by the temperature and fuel droplet distributions at the phase $\phi = 90°$ in Fig. 8(c), all the while fuel droplets have been evaporating (Fig. 8(c) right). The fuel that has evaporated during the period $\phi = 270° - 90°$ and convected downstream of the dump plane without reacting, suddenly ignites and leads to a rise in the heat release rate just prior to the phase $\phi = 180°$ (during the period $\phi = 90° - 270°$), as shown in Fig. 8(d) (right) and thus, the second larger peak of Q occurs. The temporal variation of Q in Case A-1 also has a similar double peak feature (see Fig. 6(b)), but, the magnitude of the second peak is nearly the same as that of the first peak. The reason for this reduction in magnitude of the second peak of Q compared to that in Case NA-1, is the consideration of varying degree of fuel spray atomization via. the Lee model in Case A-1. The influence of this model on fuel droplet evaporation, heat release rate and combustion instability is clarified later in the discussion that follows. It is also worth noting that interaction of flame with the wall is present, which is discernable from the FI distributions in Fig. 7 and the heat release rate distribution in Fig. 8(d). Flame-wall interaction occurs in all the cases investigated in this study. As mentioned previously in Section 2.5, the walls are assumed to be isothermal and their temperature is fixed at 760 K (same as the inlet air temperature). Therefore, as in any practical combustor, heat loss to the walls is considered in the present LESs, even though the isothermal wall boundary condition is a simplification.

Figures 9 and 10 show the spectra of pressure oscillations and the streamwise distributions of the amplitude of peak frequency components of pressure oscillations, respectively, for Case NA-1 and Case A-1. The locations A, B, and C shown in Fig. 10 correspond to the same locations shown in Fig. 4. The sampling time and period for calculating the statistics are approximately 0.05 s and 0.02 ms, respectively. Figure 9 shows that the spectra of pressure oscillations for Cases NA-1 and A-1 have a clear peak at 699 Hz, and that the peak amplitude is larger for Case NA-1. Moreover, Fig. 10 shows that the oscillation mode of the pressure variations' peak frequency component occurring in Case NA-1 and Case A-1, consists of the combustion chamber's fundamental oscillation mode (1/4 wavelength mode), with the oscillation antinode occur-
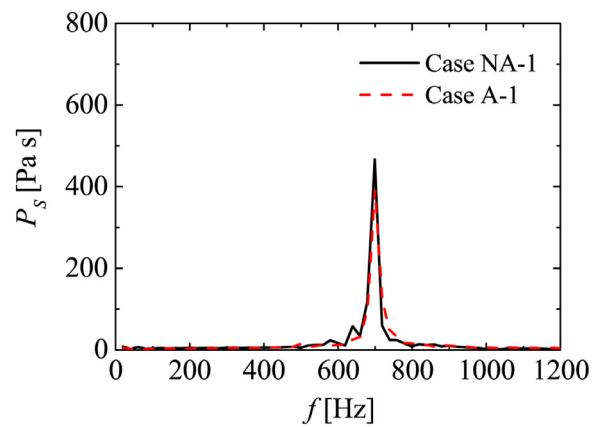

Fig. 9. Comparison of the spectra of pressure oscillations between cases without (Case NA-1) and with (Case A-1) SMD modulation.
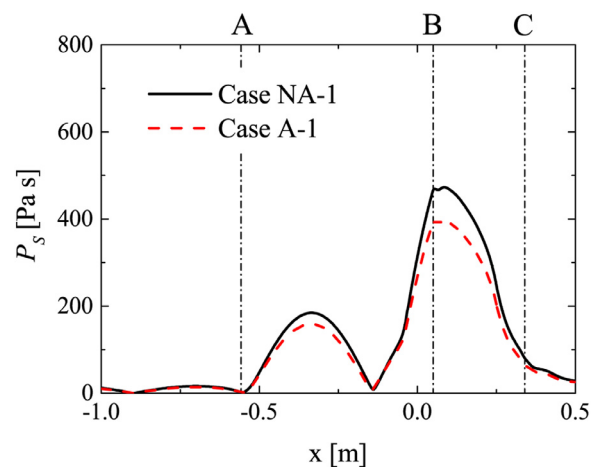

Fig. 10. Comparison of the streamwise profiles of amplitude of peak frequency components of pressure oscillations, between cases without (Case NA-1) and with (Case A-1) SMD modulation.
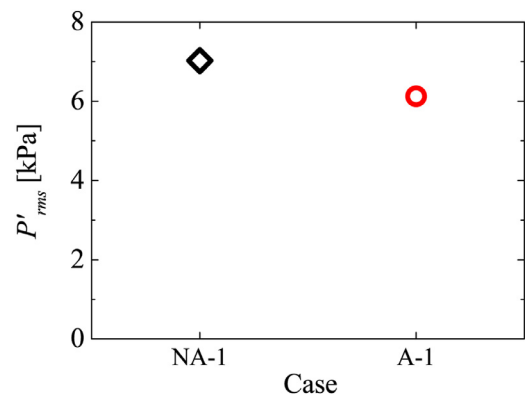

Fig. 11. Comparison of the intensities of pressure oscillations P'_{rms}, between cases without (Case NA-1) and with (Case A-1) SMD modulation.

ring at B and the oscillation node occurring at C. These results indicate that combustion instabilities indeed occur in both Case NA-1 and Case A-1. Next, the effect of time variations of the liquid fuel droplet diameter distribution upon injection, which are considered via. the Lee model, on the intensity of the pressure oscillations caused by combustion instability is investigated. Figure 11 presents the root mean square (RMS) values of pressure fluctuations in Case NA-1 and Case A-1. The figure shows that the RMS value of pres-
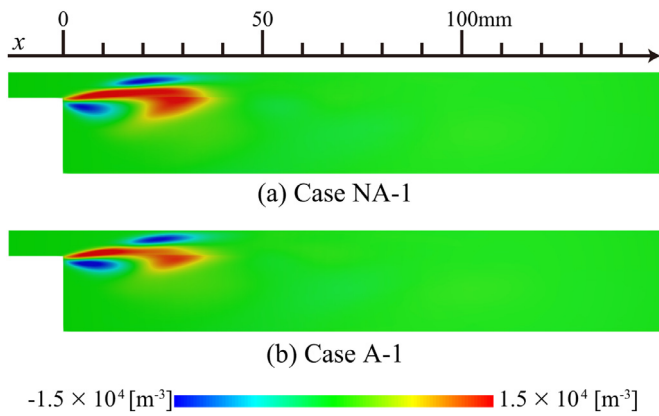
Fig. 12. Comparison of distributions of the spanwise-averaged local Rayleigh Index RI on the $x − y$ plane, between cases without (Case NA-1) and with (Case A-1) SMD modulation.
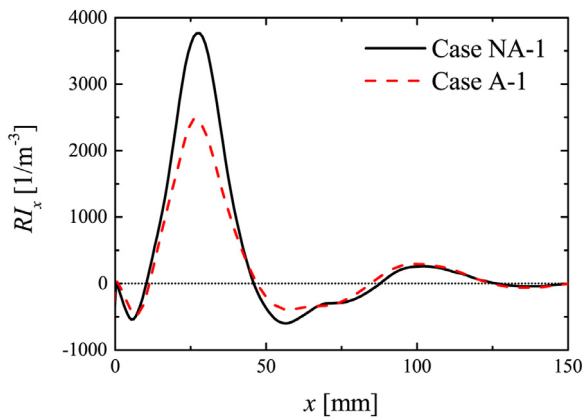

Fig. 13. Comparison of streamwise distributions of the cross-sectional $(y − z)$-averaged local Rayleigh Index RI_x, between cases without (Case NA-1) and with (Case A-1) SMD modulation.

Fig. 14. Comparison of the streamwise distributions of phase- and cross-sectional $(y − z$ plane) averaged heat release rate Q_x, at phase of $\phi = 90°$ (when $P = P_{max}$) between cases without (Case NA-1) and with (Case A-1) SMD modulation.

Fig. 15. Comparison of the streamwise distributions of phase- and cross-sectional $(y − z$ plane)-averaged evaporation rate $\dot{m}_x$, at phase of $\phi = 0°$ between cases without (Case NA-1) and with (Case A-1) SMD modulation.

sure fluctuations in Case NA-1 is approximately 10% larger in comparison with that in Case A-1. It is apparent that the time variations of the liquid fuel droplet diameter distribution upon injection (considered using the Lee model), influence the intensity of combustion instability. To identify the factors causing the difference in the RMS values of pressure fluctuations, the Rayleigh Index (RI) has been computed for each case. Here, the RI is defined as follows

$$RI = \frac{1}{t_s} \int \frac{P'q'}{P'_{rms}Q_{ave}} \, dt. \tag{10}$$

where P' and q' represent the fluctuations in pressure P and heat release rate Q, respectively, Q_{ave} represents the time-averaged value of total heat release rate inside the combustor, t_s represents the sampling time, and P'_{rms} represents the RMS value of pressure fluctuations. In the regions where RI is positive, the pressure oscillations are driven by the heat release, whereas, in the regions where RI is negative, the pressure oscillations are damped by the heat release. The $x − y$ planar distributions of spanwise-averaged (z-direction) value of local RI for Case NA-1 and Case A-1 are shown in Fig. 12, while the streamwise (x-direction) distributions of the cross-sectional $(y − z)$-averaged value of Rayleigh Index RI_x are shown in Fig. 13. Figure 12 shows that the value of RI is positive in the region near the combustion chamber's dump plane, for both Case NA-1 and Case A-1. This indicates that the pressure oscillations are driven by the heat release in this region. Additionally, Fig. 13 shows that RI_x is smaller in the vicinity of the position at a distance of $x = 25$ mm from the combustion chamber's dump plane, for Case A-1 in comparison with Case NA-1. This is the rea-
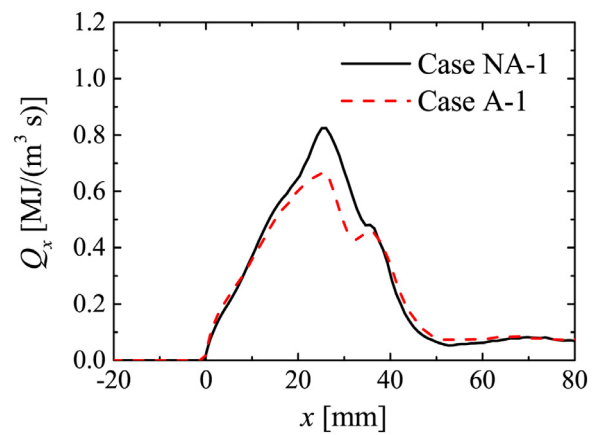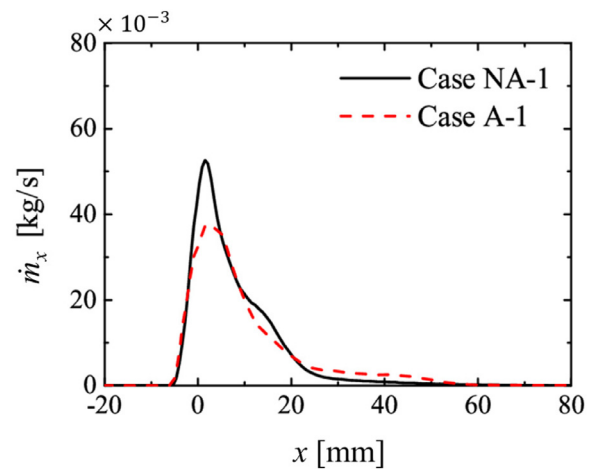
son for the RMS value of pressure oscillations in Case NA-1 being larger than that in Case A-1.

Next, the reason for the difference in the distributions of RI_x is investigated in further detail. The positive RI_x distributions are strongly influenced by the heat release rate at the phase when pressure reaches its maximum value i.e., $\phi = 90°$. The streamwise distributions of the $y − z$ cross-sectional-averaged heat release rate Q_x with phase averaging at the phase $\phi = 90°$ when pressure reaches its maximum value ($P = P_{max}$), are shown in Fig. 14 for Case NA-1 and Case A-1. The figure shows that the heat release rate at the phase when pressure is at its maxima, is greater in Case NA-1. The distribution of heat release rate at a particular phase is influenced by the distribution of evaporation rate of the fuel droplets immediately beforehand. Therefore, the streamwise distributions of the $y − z$ cross-sectional-averaged evaporation rate $\dot{m}_x$, with phase averaging at $\phi = 0°$ are shown in Fig. 15 for Cases NA-1 and A-1.

Figure 15 shows that the evaporation rate at the phase before the phase when pressure reaches its maximum value (see Fig. 6(a)), is higher for Case NA-1 in comparison with Case A-1. Moreover, the figure also shows that the fuel droplets evaporate mostly in the vicinity of the dump plane above the step (near $x = 0$ mm). The behavior of fuel droplets after being injected was investigated in detail by post-processing the LES data. The results revealed that the fuel droplets required approximately one half of a
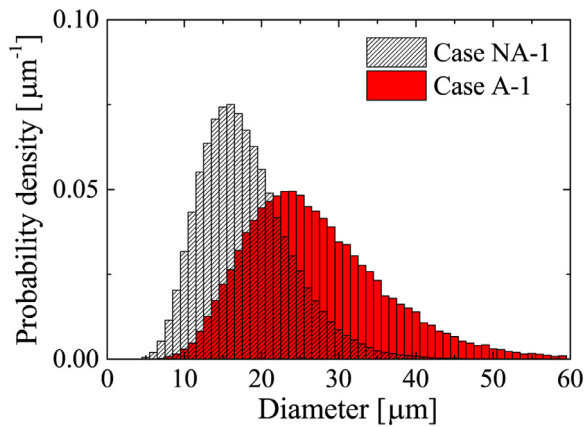
Fig. 16. Comparison of phase-averaged fuel droplet size distributions at the phase of $\phi = 180°$, between cases without (Case NA-1) and with (Case A-1) SMD modulation.

period (i.e., phase difference of 180°) to traverse from the fuel injection ports to the location directly above the step/dump plane (distance of 5 mm). Therefore, the decrease in the evaporation rate at phase $\phi = 0°$ in Case A-1 is influenced by the droplet diameter distribution of the injected liquid fuel, at the phase that occurs approximately one half of a period earlier (in other words, at $\phi = 180°$).

Figure 16 shows the Probability Density Functions (PDF) of droplet diameter distribution of the injected liquid fuel droplets, with phase averaging at $\phi = 180°$ for Case NA-1 and Case A-1. The figure shows that the number of fuel droplets with large diameters at $\phi = 180°$ increased in Case A-1 in comparison with Case NA-1. As mentioned previously, the SMD and hence, the size distribution of injected fuel droplets are fixed in time for Case NA-1, while they vary in time for Case A-1. The fuel injection rate at any given phase is the same in both cases, meaning the volume of fuel injected is the same. However, the total droplet surface area available for evaporation is different between these two cases, which follows from the fundamental definition of Sauter Mean Diameter. For a fixed volume of fuel spray injected, its total surface area is inversely proportional to the SMD. Therefore, a shift to larger SMD implies a decrease in the total surface area available for evaporation. Therefore, the injection of relatively larger fuel droplets at phase $\phi = 180°$ in Case A-1, leads to a reduction in the peak evaporation rate near the dump plane at the subsequent phase of $\phi = 0°$ (see Fig. 15).

These results reveal that the temporal fluctuations of liquid fuel droplet size distribution (considered using the atomization/Lee model in Case A-1), which are caused by the velocity fluctuations of incoming air that accompanies the combustion instability, lead to the injection of fuel droplets with larger diameters in Case A-1, even though the mass/volume of fuel injected is the same in both cases. This leads to a decrease in the evaporation rate locally, which in turn decreases the heat release rate near the dump plane at the phase when pressure reaches its maximum value. Consequently, the correlation between heat release rate fluctuations and pressure oscillations is weakened (as indicated by the difference in the RI_x distributions in Fig. 13), which decreases the intensity of combustion instability.

3.2. Influence of temporal variations of liquid fuel flow rate on combustion instability

First, it is confirmed whether or not combustion instabilities are excited in the cases where the time variations of liquid fuel flow rate are considered, but the time variations of droplet size distri-

bution are not (i.e., without SMD modulation). The phase shift ϕ_{ph} between the fuel flow rate variations and the pressure oscillations (used in the VMFR model) in Cases NA-2, NA-3, NA-4, and NA-5 is set to 0°, 90°, 180°, and 270°, respectively. Figure 17 shows the time variations of pressure P, heat release rate Q, streamwise velocity $\tilde{u}$, fuel droplet evaporation rate $\dot{m}$, and Fuel Mass Flow Rate (Fuel M.F.R) for Cases NA-2, NA-3, NA-4, and NA-5. The quantities P, $\tilde{u}$, Q and $\dot{m}$ shown in the figure are defined the same way as those in Fig. 6(a) and (b) of Section 3.1. The new quantity appearing in Fig. 17 is Fuel M.F.R (Mass Flow Rate) which represents the total value of fuel injection rate from all 7 ports. Figure 17 shows that these various physical quantities clearly oscillate with a period that is approximately constant in each case, except for Case NA-2. The phase difference between the variations of P and $\tilde{u}$ is approximately 90° in all cases except for Case NA-2. Moreover, the figure also shows that in all cases, the peaks in the variations of Fuel M.F.R occur approximately at 180° ~ 270° after the peaks in the variations of $\dot{m}$. Additionally, the phase shift between the variations of fuel flow rate and that of pressure, matches the value of phase difference ϕ_{ph} set for all the cases (see Table 1).

Figures 18 and 19 illustrate the pressure oscillation spectra and the streamwise distributions of the peak frequency component amplitudes of the pressure oscillations, respectively, for all the cases. The locations A, B, and C in Fig. 19 correspond to the same locations as shown in Fig. 4. The sampling time and period for calculating the statistics are approximately 0.05 s and 0.02 ms, respectively. Figure 18 shows that for all cases, the spectra of pressure oscillations have clear peaks within the frequency range of 600 Hz–750 Hz, and that the frequency corresponding to peak amplitude becomes smaller, as the phase shift ϕ_{ph} applied to the fuel flow rate variations becomes larger. Additionally, Fig. 19 shows that the oscillation mode of the peak frequency component of the pressure variations occurring in all cases, consists of the fundamental oscillation mode (1/4-wavelength mode) of the combustion chamber, with the oscillation antinode occurring at B and the oscillation node occurring at C. These results reveal that combustion instabilities occur in the cases that consider the temporal fluctuations in liquid fuel flow rate.

The effect of liquid fuel flow rate fluctuations accounted for by the VMFR (Variable Mass Flow Rate) model, on the intensity of pressure oscillations arising from combustion instabilities is investigated next. In Case NA-5, flashback (a phenomenon wherein flames and fuel droplets flow upstream) and a particularly unstable combustion instability phenomenon occurred. Therefore, only Case NA-2, Case NA-3, and Case NA-4 are primarily discussed in this section. Figure 20 shows the RMS values of the pressure oscillations for all cases. The RMS value of pressure oscillations for Case NA-1, wherein the VMFR model is not applied, is also plotted for comparison. The figure shows that the phase shift ϕ_{ph} applied between the fluctuations in liquid fuel flow rate and the pressure oscillations using the VMFR model, influences the RMS value of the pressure oscillations (and hence, the intensity of combustion instabilities). It is evident that, as the phase shift ϕ_{ph} applied to the fuel flow rate fluctuations increases, the RMS value of pressure oscillations also increases. It is also apparent from Fig. 17 that, as the value of phase shift ϕ_{ph} increases, the amplitude of fuel mass flow rate (Fuel M. F. R) fluctuations also increases, which would influence the local fuel droplet evaporation rate. This would in turn influence the heat release rate, and consequently the coupling between heat release rate fluctuations and pressure oscillations, which would ultimately dictate the intensity of combustion instabilities. These factors are discussed in detail in the following.
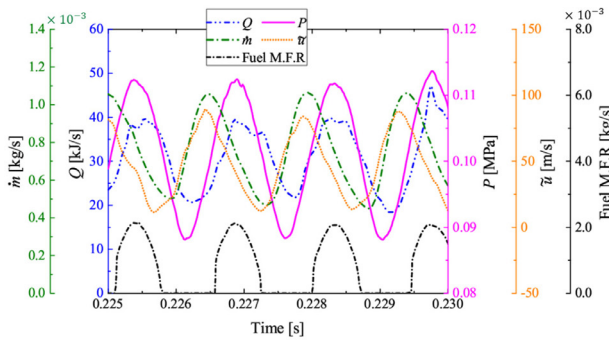
To investigate the factors causing this increase in the RMS value of pressure oscillations, the Rayleigh Index RI for each case is calculated. Figure 21 shows the $x - y$ planar distributions of the spanwise-averaged (z-direction) value of RI for each case. The fig-
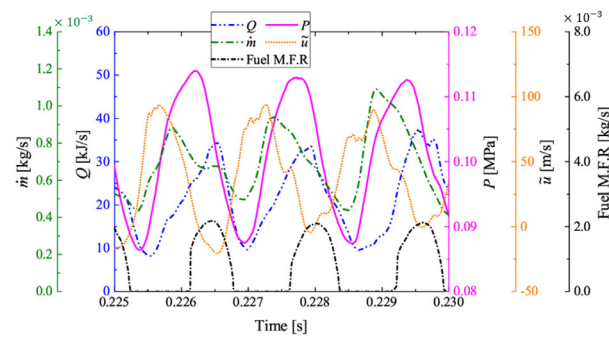
A.L. Pillai, J. Nagao and R. Awane et al./Combustion and Flame 220 (2020) 337–356
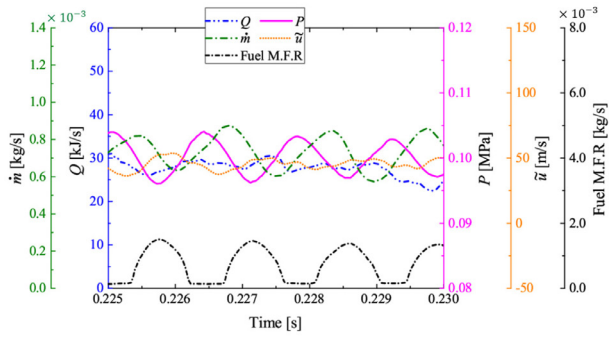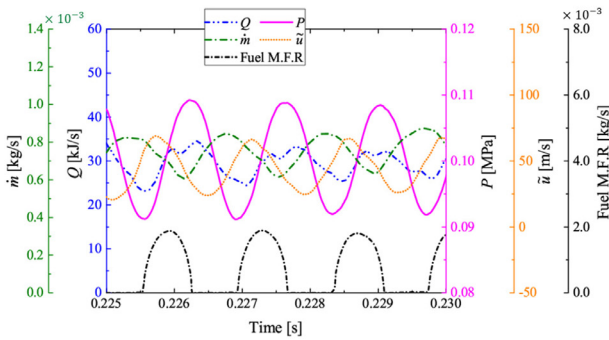
(a) Case NA-2

(b) Case NA-3

(c) Case NA-4

(d) Case NA-5

Fig. 17. Comparisons of time variations of pressure P, heat release rate Q, streamwise velocity $\tilde{u}$, droplet evaporation rate $\dot{m}$, and fuel mass flow rate (Fuel M.F.R), among cases with different phase shift angle ϕ_{ph} and without SMD modulation (Cases NA-2 to NA-5).
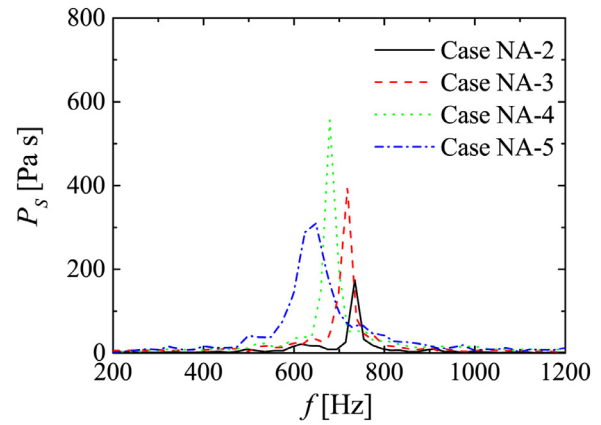
Fig. 18. Comparison of the spectra of pressure oscillations among cases with different phase shift angle ϕ_{ph} and without SMD modulation (Cases NA-2 to NA-5).
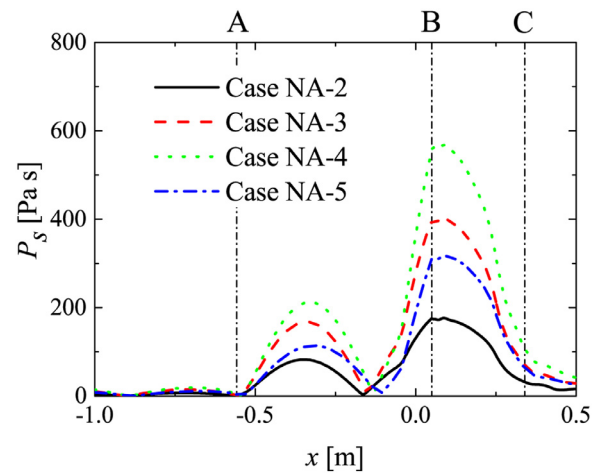
Fig. 19. Comparison of the streamwise profiles of amplitude of peak frequency components of pressure oscillations, among cases with different phase shift angle ϕ_{ph} and without SMD modulation (Cases NA-2 to NA-5).
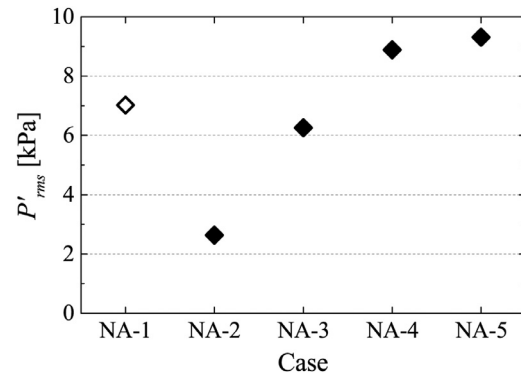
Fig. 20. Comparison of the intensities of pressure oscillations P'_{rms}, among cases with different phase shift angle ϕ_{ph} and without SMD modulation (Cases NA-1 to NA-5).

ure shows that as the phase shift ϕ_{ph} increases, the region in which the RI is positive becomes larger, and the region wherein RI is negative becomes smaller. Figure 22 shows the streamwise distributions of RI_x, which is the cross-sectional $(y − z)$-averaged value of the RI, for each case. The figure shows that in Case NA-2, Case NA-3, and Case NA-4, the positive peak position of RI_x approaches the vicinity of the combustion chamber's dump plane (upstream side) as the phase shift ϕ_{ph} increases. The antinodes
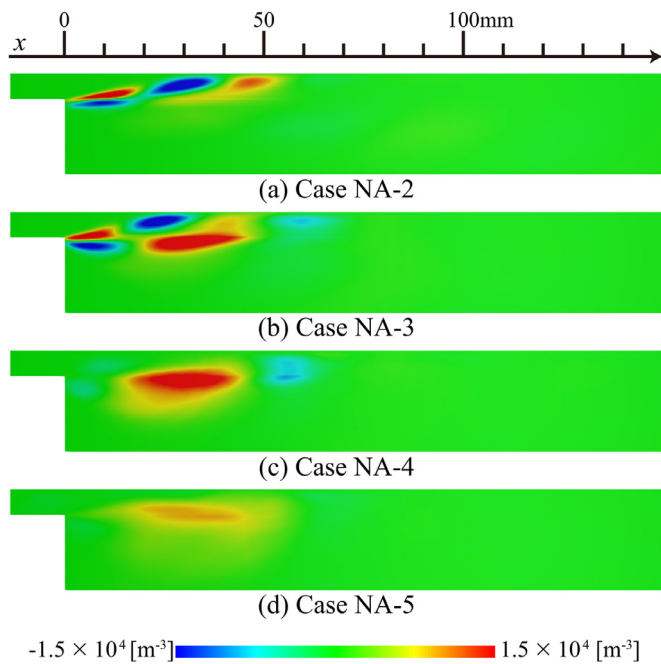
Fig. 21. Comparison of distributions of the spanwise-averaged local Rayleigh Index on the $x - y$ plane, among cases with different phase shift angle ϕ_{ph} and without SMD modulation (Cases NA-2 to NA-5).
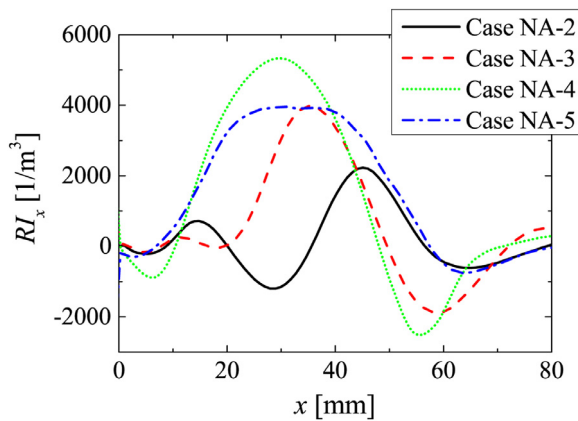

Fig. 22. Comparison of the streamwise distributions of cross-sectional $(y - z)$-averaged local Rayleigh Index RI_x, among cases with different phase shift angle ϕ_{ph} and without SMD modulation (Cases NA-2 to NA-5).

Fig. 23. Comparison of the streamwise distributions of phase- and cross-sectional $(y - z)$-averaged local heat release rate Q_x, at the phase of $\phi = 90°$ among cases with different phase shift angle ϕ_{ph} and without SMD modulation (Cases NA-2 to NA-4).

Fig. 24. Comparison of the streamwise distributions of phase-averaged local fuel mass M_x, at the phase of $\phi = 0°$ among cases with different phase shift angle ϕ_{ph} and without SMD modulation (Cases NA-2 to NA-4).

of pressure oscillations corresponding to the peak frequency components of Cases NA-2 to NA-5 are located near the combustor's dump plane, as shown in Fig. 19. Therefore, the positive peak of RI_x shifting upstream, closer to the dump plane would enhance the pressure oscillation amplitude. Hence, the difference in the RI_x distributions among Cases NA-2 to NA-5 is the reason behind the increasing RMS value of pressure oscillations, with increasing phase shift ϕ_{ph} applied to the temporal fluctuations of liquid fuel flow rate.

Next, the reasons for the differences in the distributions of RI_x are investigated in further detail. The positive RI_x distributions are strongly influenced by the heat release rate at the phase when pressure reaches its maximum value ($\phi = 90°$). The streamwise distributions of the cross-sectional $(y - z)$-averaged heat release rate Q_x, with phase averaging at the phase $\phi = 90°$ (when $P = P_{max}$), are shown in Fig. 23 for Case NA-2, Case NA-3, and Case NA-4. The figure shows that as the phase shift ϕ_{ph} increases, the peak value of Q_x distribution also increases and its position moves
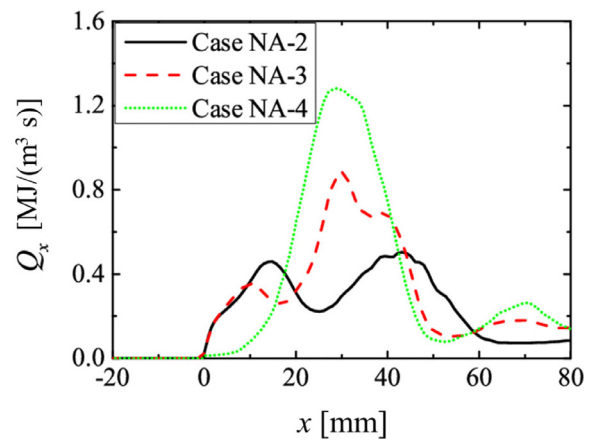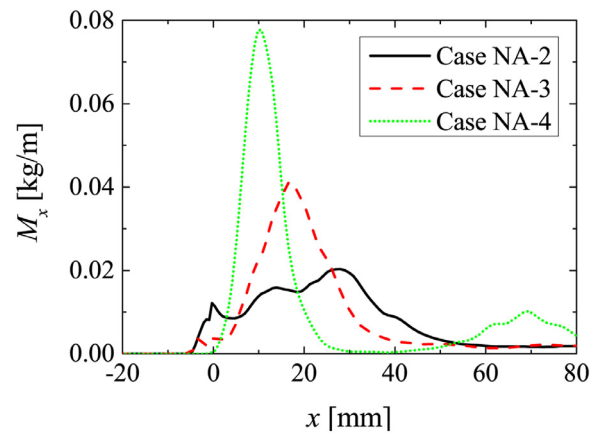
upstream. Moreover, the position of the peak in Q_x distribution approximately coincides with the position of positive peak in the RI_x distribution for each case (see Fig. 22). Therefore, the fact that the position of peak in the heat release rate at the phase when pressure reaches its maximum value, is moving upstream as the phase shift ϕ_{ph} applied to the fluctuations of liquid fuel flow rate increases, is the reason for the difference in the RI_x distributions.

In the following, reasons for the upstream shift in the position of peak heat release rate (i.e., peak values of Q_x distributions in Fig. 23) at the phase when pressure reaches its maximum value (i.e., $\phi = 90°$), with increasing phase shift ϕ_{ph} are investigated further. The spatial distribution of heat release rate at a particular phase (or time instance) is strongly influenced by the spatial distribution of gaseous fuel at the phase occurring immediately beforehand. Therefore, the streamwise distributions of the gaseous fuel mass M_x with phase averaging at $\phi = 0°$, which will dictate the distributions of Q_x at phase $\phi = 90°$, are shown in Fig. 24 for Case NA-2, Case NA-3, and Case NA-4. The figure shows that as the phase shift ϕ_{ph} increases, the peak value of M_x also increases and its position moves upstream. The distribution of the gaseous fuel at a particular phase is also strongly influenced by the distribution of fuel droplet evaporation rate at the phase occurring immediately beforehand. Hence, the streamwise distributions of the cross-sectional $(y - z)$-averaged evaporation rate $\dot{m}_x$ with phase
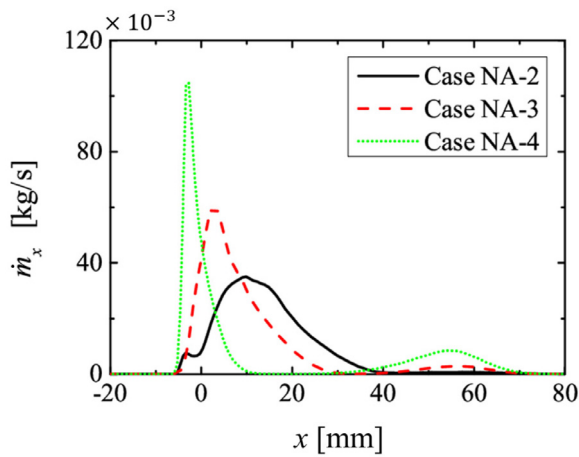
Fig. 25. Comparison of the streamwise distributions of phase- and cross-sectional $(y - z)$-averaged local evaporation rate $\dot{m}_x$, at the phase of $\phi = 270°$ among cases with different phase shift angle ϕ_{ph} and without SMD modulation (Cases NA-2 to NA-4).

averaging at $\phi = 270°$, which will govern the distributions of M_x at $\phi = 0°$, are shown in Fig. 25 for Case NA-2, Case NA-3, and Case NA-4. Similar to the trends in the distributions of Q_x and M_x, the figure shows that as the phase shift ϕ_{ph} that is applied to the time variations of the liquid fuel flow rate increases, the peak value of $\dot{m}_x$ increases, its position moves upstream, and becomes more localized. Therefore, the reason for the position of peak heat release rate moving towards the upstream side of the combustor with increasing phase shift ϕ_{ph}, is the change in the relationship between the phase of temporal fluctuations of the liquid fuel flow rate, and the phase of time variations of the incoming oxidizing air's streamwise velocity, that leads to an increase in the residence time of the fuel droplets in the vicinity of the combustor's dump plane, causing an increase in the supply of gaseous fuel at the phase when pressure reaches its maximum value.

The results presented above indicate that the flow rate time variations of the liquid fuel injected into the combustion chamber, have a strong influence on the intensity of combustion instability. Moreover, as the phase shift ϕ_{ph} between the fuel flow rate variations and the pressure oscillations increases, the intensity of combustion instability also increases. This is due to the fact that the residence time and local evaporation rate of the fuel droplets increase as the phase shift ϕ_{ph} increases, which causes an increase in the heat release rate in the vicinity of the combustion chamber's dump plane, and also increases the strength of the correlation between the heat release rate fluctuations and the pressure oscillations.

3.3. Influences of temporal variations of droplet diameter distribution and liquid fuel flow rate on combustion instability

The excitation of combustion instabilities in the cases where temporal variations of both the fuel droplet diameter distribution (atomization/Lee model) and the fuel flow rate (VMFR model) are considered, is first confirmed. The phase shift ϕ_{ph} between the fuel flow rate variations and the pressure oscillations in Cases A-2, A-3, A-4, and A-5 is set to $0°$, $90°$, $180°$, and $270°$, respectively. Figure 26 shows the time variations of pressure P, heat release rate Q, streamwise velocity $\tilde{u}$, fuel droplet evaporation rate $\dot{m}$, SMD (Sauter Mean Diameter), and Fuel M.F.R for Cases A-2, A-3, A-4, and A-5. Once again, these quantities bear the same definitions as those in Figs. 6 and 17 of Sections 3.1 and 3.2, respectively. Figure 26 shows that these various physical quantities oscillate with a period that is approximately constant in each case, and
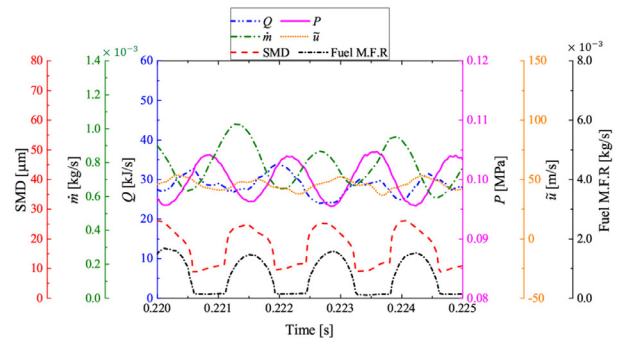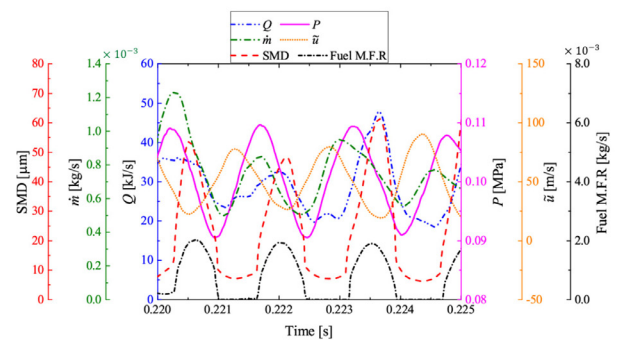

(a) Case A-2
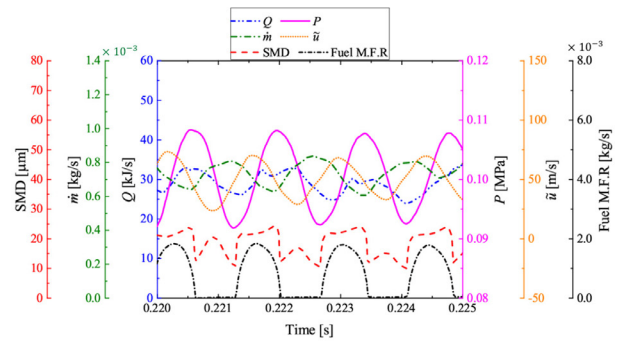
(b) Case A-3
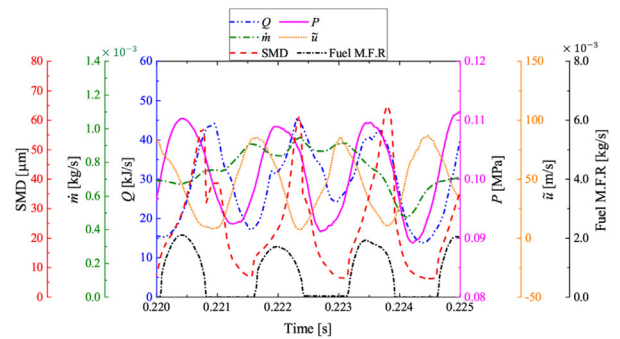
(c) Case A-4

(d) Case A-5

Fig. 26. Comparisons of time variations of pressure P, heat release rate Q, streamwise velocity $\tilde{u}$, droplet evaporation rate $\dot{m}$, droplet Sauter Mean Diameter (SMD), and fuel mass flow rate (Fuel M.F.R), among cases with different phase shift angle ϕ_{ph} and with SMD modulation (Cases A-2 to A-5).
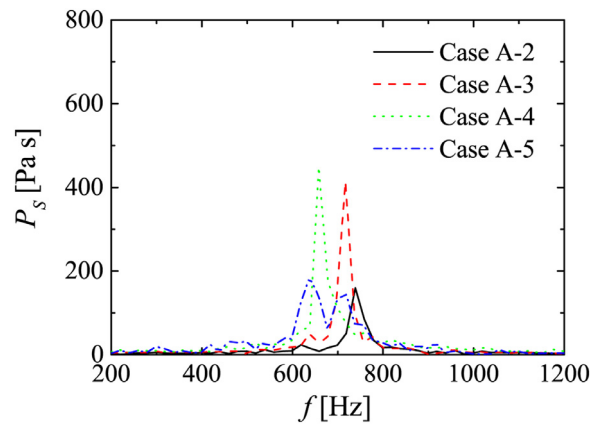
Fig. 27. Comparison of the spectra of pressure oscillations among cases with different phase shift angle ϕ_{ph}, and with SMD modulation (Cases A-2 to A-5).
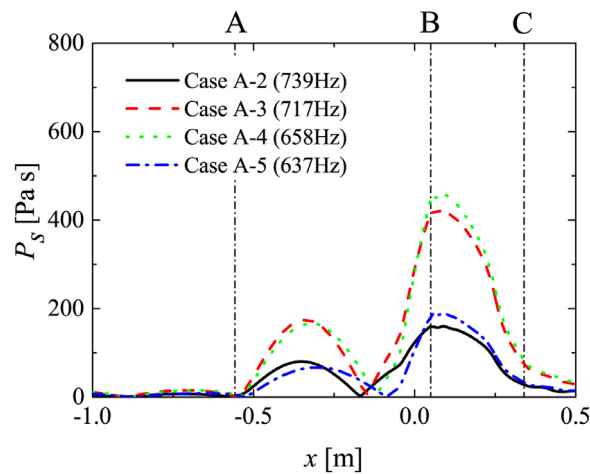

Fig. 29. Comparison of the intensities of pressure oscillations P'_{rms}, among cases with different phase shift angle ϕ_{ph}, without (Cases NA-1 to NA-5) and with (Cases A-1 to A-5) SMD modulation.

Fig. 28. Comparison of streamwise profiles of the amplitude of peak frequency components of pressure oscillations, among cases with different phase shift angle ϕ_{ph} and with SMD modulation (Cases A-2 to A-5).

that combustion instabilities are excited in all cases. Moreover, the phase difference between the variations of P and $\tilde{u}$ is 90°. Additionally, the phase shifts ϕ_{ph} between the variations of fuel flow rate and the pressure oscillations match the settings in Table 1.

Figures 27, 28, and 29 show the spectra of pressure oscillations, the streamwise distributions of the amplitude of peak frequency components of the pressure oscillations, and the intensity of pressure oscillations P'_{rms}, respectively, for Cases A-2, A-3, A-4, and A-5 (Fig. 29 also shows the comparison of P'_{rms} with Case A-1 and the cases without SMD modulation i.e., Cases NA-1 to NA-5). Locations A, B, and C shown in Fig. 28 correspond to the same locations depicted in Fig. 4. The sampling time and period are approximately 0.05 s and 0.02 ms, respectively, for calculation of statistics. Figure 27 shows that the spectra of pressure oscillations have clear peaks in the frequency range of 600 Hz to 750 Hz for all cases. Additionally, Fig. 28 shows that the oscillation mode of the peak frequency component of pressure variations that occurs in all cases, consists of the fundamental oscillation mode (1/4-wavelength mode) of the combustion chamber, with the oscillation antinode and node occurring at B and C, respectively. These results indicate that combustion instabilities occur in the cases considering the time variations of both liquid fuel flow rate and fuel droplet diameter distribution (i.e., Cases A-2 to A-5).

Next, the effects of time variations of droplet diameter distribution and liquid fuel flow rate (i.e., when both variations
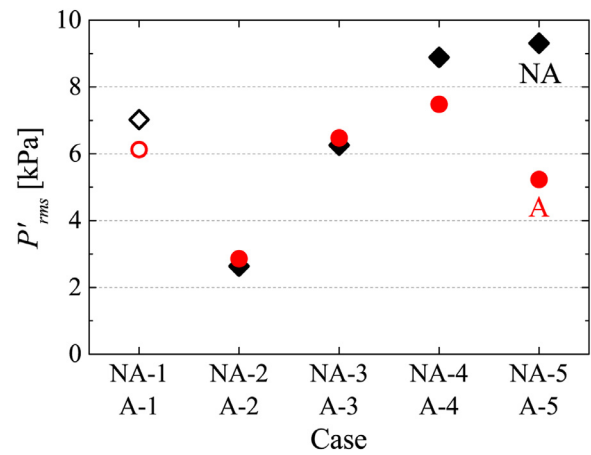
are considered simultaneously), on the intensity of pressure oscillations caused by the combustion instabilities are investigated. Figure 29 shows the RMS values of pressure oscillations P'_{rms} for all cases (including the ones in which the Lee model is not used). The RMS values of pressure oscillations for Case NA-1 and Case A-1, wherein the VMFR model is not applied, are also plotted for comparison. The figure shows that, contrary to the trend for the cases in which only the time variations of fuel flow rate are considered (i.e., Cases NA-2 to NA-5 wherein only the VMFR model is applied, but not the Lee model), Cases A-4 and A-5 show an opposite trend in the intensity of pressure oscillations (P'_{rms}) with increasing ϕ_{ph}. In these cases, the temporal fluctuations of fuel droplet diameter distribution (considered using the Lee/atomization model) have the effect of decreasing the pressure oscillation intensity P'_{rms} (and hence the intensity of combustion instabilities), upon its mutual interaction with the fluctuations in liquid fuel flow rate (VMFR model). Additionally, as the phase shift ϕ_{ph} between the temporal fluctuations in fuel flow rate and the pressure oscillations becomes larger, the effect of the temporal fluctuations of fuel droplet diameter distribution on reducing P'_{rms} becomes more pronounced.

In the following, reasons for the reduction in the values of P'_{rms} at larger values of phase shift ϕ_{ph}, due to the influence of fluctuations in fuel droplet diameter distribution, and its interaction with the fluctuations in fuel flow rate are investigated. Figure 30 shows the $x - y$ planar distributions of the spanwise-averaged (z-direction) value of the Rayleigh Index RI for each case. By comparing Figs. 21 and 30, it can be seen that for the cases in which the phase shift ϕ_{ph} is large, i.e., Case A-4 ($\phi_{ph} = 180°$) and Case A-5 ($\phi_{ph} = 270°$), the region wherein RI is positive becomes smaller compared to that in the planar distributions of spanwise-averaged RI of the corresponding cases in Fig. 21 (i.e., Case NA-4 and Case NA-5, respectively, with corresponding phase shifts ϕ_{ph}). This difference in the RI distributions causes the pressure oscillations' RMS value to become smaller in Case A-4 and Case A-5. However, from Figs. 21 and 30, it is evident that the distributions of RI in Case A-2 and Case A-3 are virtually the same as those in Case NA-2 and Case NA-3, respectively. But, the intensity of pressure oscillations P'_{rms} of Case A-2 and Case A-3 are marginally higher than those of the corresponding cases without the Lee model (without SMD modulation), i.e., Case NA-2 and Case NA-3 as shown in Fig. 29. The phase shift ϕ_{ph} applied to Cases NA-2 and A-2 is $\phi_{ph} = 0°$, and that applied to Cases NA-3 and A-3 is a relatively small value of $\phi_{ph} = 90°$. Figure 31 illustrates the comparison of streamwise distributions of cross-sectional ($y - z$)-averaged local Rayleigh Index RI_x between Cases NA-2 and A-2, and between Cases NA-3 and A-3. The RI_x dis-
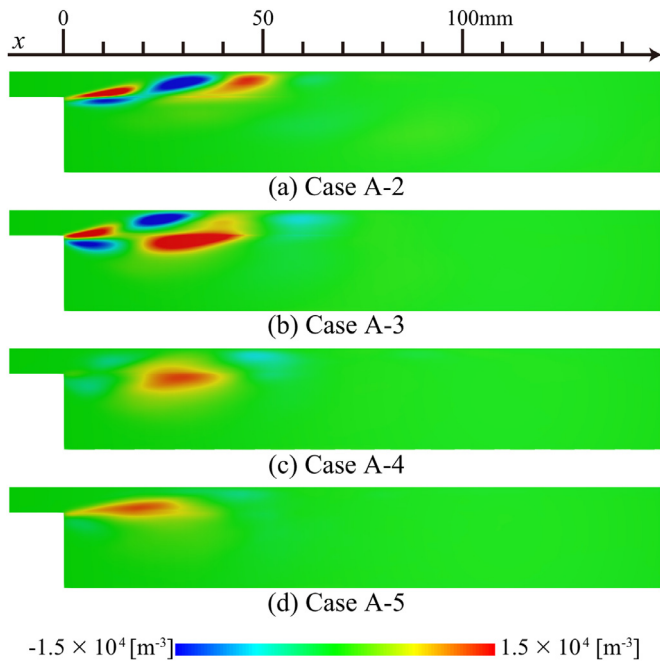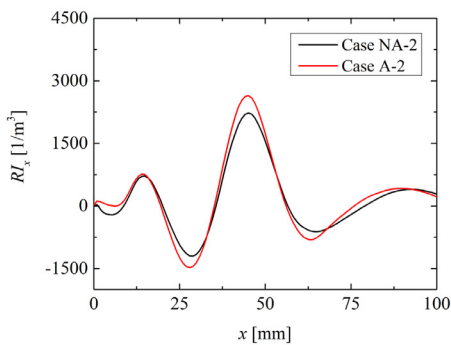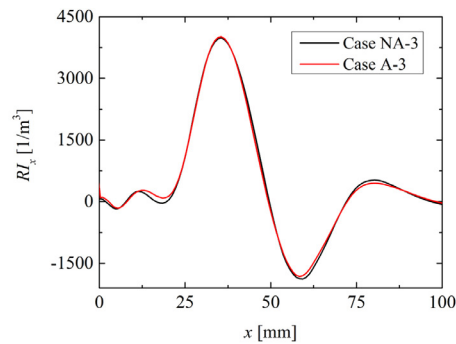
Fig. 30. Comparison of distributions of the spanwise-averaged local Rayleigh Index on the x-y plane, among cases with different phase shift angle ϕ_{ph}, and with SMD modulation (Cases A-2 to A-5).

Fig. 32. Comparison of the streamwise distributions of phase- and cross-sectional (y-z)-averaged heat release rate Q_x, at the phase of $\phi = 90°$ (when $P = P_{max}$), between cases without (Case NA-4) and with (Case A-4) SMD modulation.

tributions of Cases NA-2 and A-2 in Fig. 31(a) are similar in shape, but the positive RI_x distribution of Case A-2 has slightly larger values at certain streamwise locations, especially close to the dump plane. Similar tendency is observed in the RI_x distributions of Cases NA-3 and A-3 in Fig. 31(b). In the vicinity of the dump plane, the positive RI_x distribution of Case A-3 also has slightly larger values compared to that of Case NA-3. Therefore, the P'_{rms} values of Case A-2 and Case A-3 are marginally higher (although the difference is virtually insignificant) than those of the corresponding cases without the Lee model (without SMD modulation), i.e., Case NA-2 and Case NA-3, respectively.

The cause for the RMS value of pressure oscillations in Case A-4 being smaller than that in Case NA-4 is examined next. Since the positive RI spatial distributions are strongly influenced by the heat release rate at the phase when pressure reaches its maximum value (i.e., $\phi = 90°$), the streamwise distributions of the cross-sectional ($y - z$)-averaged heat release rate Q_x with phase averaging at the phase $\phi = 90°$ are shown in Fig. 32 for Cases NA-

4 and A-4. The figure shows that the value of Q_x in the vicinity of the combustion chamber's dump plane is smaller in Case A-4 compared to Case NA-4. The distribution of heat release rate at $\phi = 90°$ is governed by the distribution of fuel droplet evaporation rate at the phase occurring previously. Hence, the $x - y$ planar distributions of phase- and spanwise-averaged (z-direction) fuel droplet evaporation rate $\dot{m}_x$ at various phases are examined in Fig. 33 for Cases NA-4 and A-4. The figure shows that the evaporation rate in the vicinity of the combustor's dump plane is smaller for Case A-4 in comparison with Case NA-4 during $\phi = 270° - 0°$. Therefore, the decrease in heat release rate at phase $\phi = 90°$ in Case A-4 is caused by the decrease in its evaporation rate during $\phi = 270° - 0°$.

The behavior of fuel droplets after being injected was analyzed in detail by post-processing the LES data, to investigate the reason behind the decrease in evaporation rate during $\phi = 270° - 0°$ in Case A-4. The results revealed that many of the droplets in the region where the evaporation rate for Case A-4 was lower in comparison with Case NA-4 during $\phi = 270° - 0°$, were injected at phase $\phi \approx 90°$ when the fuel mass flow rate is largest (this can be confirmed from Figs. 17(c) and 26(c)). In Cases NA-4 and A-4, fuel injection starts around $\phi = 0°$ and lasts up to $\phi = 180°$, with the fuel injection rate peaking at $\phi \approx 90°$ (see Figs. 17(c) and 26(c), respectively). Furthermore, the inlet air mass flow rate is fixed in both cases and the overall equivalence ratio is also maintained at 1.0 in both cases. From Fig. 26(c), it is evident that the
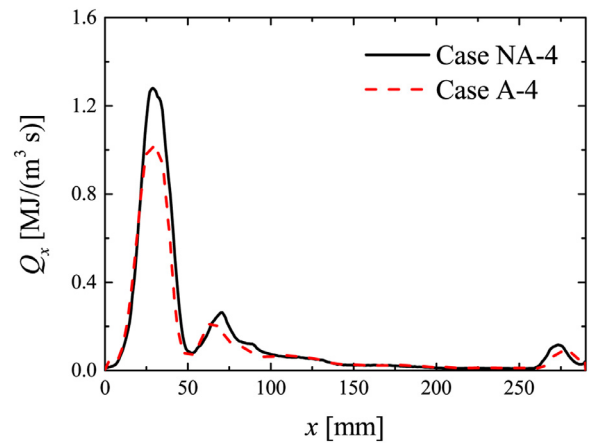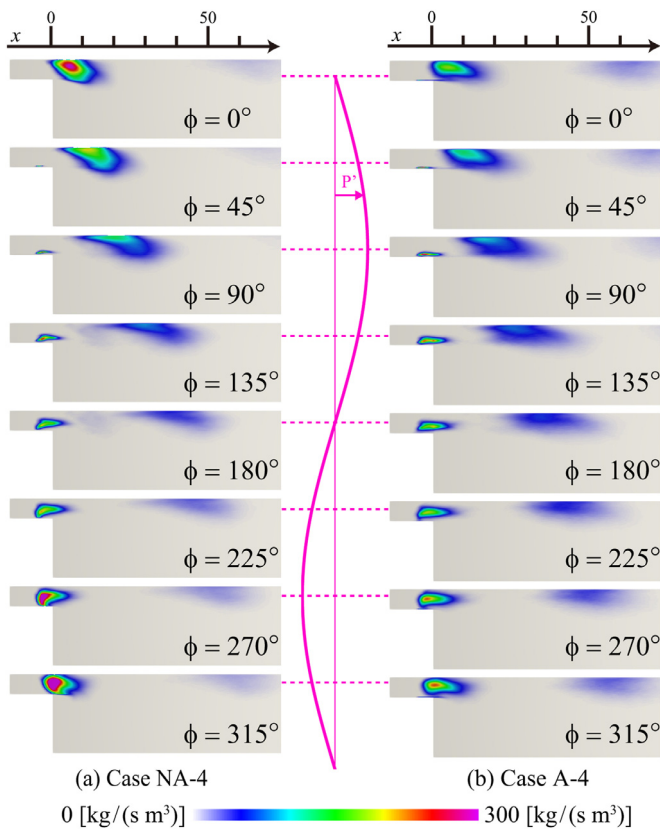

Fig. 31. Comparison of the streamwise distributions of cross-sectional ($y - z$)-averaged local Rayleigh Index RI_x between (a) Cases NA-2 and A-2, and (b) Cases NA-3 and A-3.

Fig. 34. Comparison of phase-averaged droplet size distributions, at the phase of $\phi = 90°$ (when $P = P_{max}$), between cases without (Case NA-4) and with (Case A-4) SMD modulation.

Fig. 33. Comparison of the distributions of phase- and spanwise-averaged evaporation rate, between cases without (Case NA-4) and with (Case A-4) SMD modulation.

Fig. 35. Comparison of the streamwise distributions of phase- and cross-sectional (y-z)-averaged heat release rate Q_x, at the phase of $\phi = 90°$ (when $P = P_{max}$), between cases without (Case NA-5) and with (Case A-5) SMD modulation.

SMD of injected fuel spray in Case A-4 is mostly large compared to the constant SMD value of 22.5 μm of the injected fuel spray in Case NA-4, during the fuel injection period of $\phi = 0° - 180°$. The total mass/volume of fuel spray injected during the period $\phi = 0° - 180°$ is nearly the same in both Cases NA-4 and A-4, but in Case A-4, the injected spray comprises of larger diameter droplets compared to Case NA-4. For the same volume of fuel spray injected, the total droplet surface area available for evaporation is inversely proportional to the SMD. The droplet relaxation time τ_d and the turbulent time scale τ_t (defined in Section 3.1) estimates for Case NA-4 are, $\tau_d = 5.72 \times 10^{-8} - 7.89 \times 10^{-4}$ s and $\tau_t = 6.04 \times 10^{-3}$ s, yielding Stokes number (defined here as the ratio τ_d/τ_t) in the range St $= 9.47 \times 10^{-6} - 0.131$. Similarly, for Case A-4, $\tau_d = 5.69 \times 10^{-8} - 8.78 \times 10^{-4}$ s and $\tau_t = 4.46 \times 10^{-3}$ s, which implies St ranges from 1.28×10^{-5} to 0.197. A lot of the fuel droplets injected during $\phi = 0° - 180°$ reside in the vicinity of the dump plane in both cases (due to the application of phase shift $\phi_{ph} = 180°$ between the fuel flow rate fluctuations and the pressure oscillations), which can be qualitatively discerned from the distributions of evaporation rate at the corresponding phases ϕ in Fig. 33 (although there will be some time delay between fuel spray injection and evaporation). Since the fuel mass flow rate is maximum at $\phi = 90°$, the decrease in fuel droplet evaporation rate in the vicinity of combustor's dump plane in Case A-4, will be influenced by the droplet diameter distribution of liquid fuel at $\phi \approx 90°$. Figure 34 shows the size distributions of fuel droplets with phase averaging at $\phi = 90°$ for Cases NA-4 and A-4. The droplet size distribution PDFs shown in this figure are computed at the phase $\phi = 90°$, using all the droplets within the control volume ranging from the fuel injection ports' location to the combustor's dump plane. This implies that the fuel droplets that were injected starting at the phase $\phi = 0°$ till the phase $\phi = 90°$,
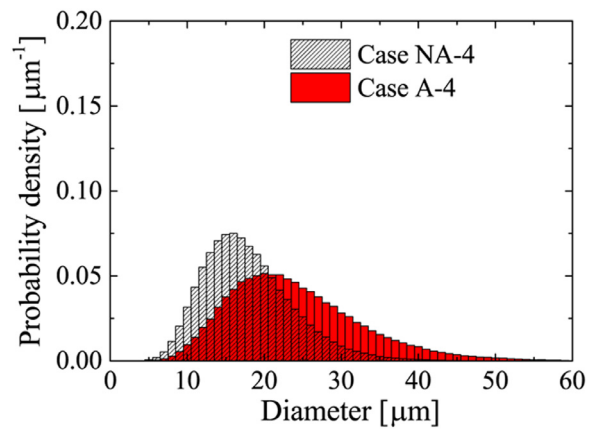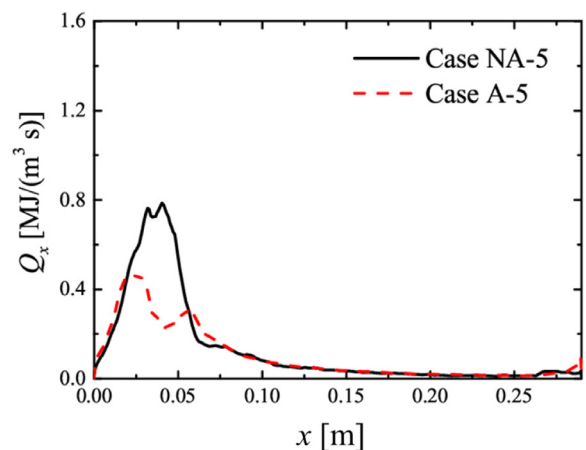
and that are still residing within the aforementioned control volume, are included in the droplet size distribution PDFs depicted in Fig. 34. This figure shows that the droplet diameter distribution becomes wider in Case A-4 at phase $\phi = 90°$, resulting in a larger SMD of the fuel spray for Case A-4. Hence, the evaporation rate near the dump plane is lower in Case A-4 compared to Case NA-4 during $\phi = 270° - 0°$. These results reveal that the reason for the RMS value of pressure oscillations becoming smaller in Case A-4, is the mean droplet diameter of the fuel spray becoming larger (owing to the application of Lee/atomization model), which subsequently causes the evaporation rate to decrease. This in turn leads to a reduction in the heat release rate in the vicinity of the combustion chamber's dump plane, that ultimately weakens the correlation between the heat release rate fluctuations and the pressure oscillations.

The reason for P'_{rms} becoming smaller for Case A-5 in comparison with Case NA-5 is also investigated. Similar to the situation between Cases A-4 and NA-4, the region wherein RI is positive becomes smaller in Case A-5 (see Fig. 30) compared to Case NA-5 (see Fig. 21), which causes the decrease in its pressure oscillation intensity P'_{rms}. Therefore, the heat release rate at the phase when pressure reaches its maximum value ($\phi = 90°$) is examined. Figure 35 shows the streamwise distributions of the cross-sectional ($y - z$)-averaged heat release rate Q_x, with phase averaging at $\phi = 90°$ for Cases NA-5 and A-5. The figure shows that the value of
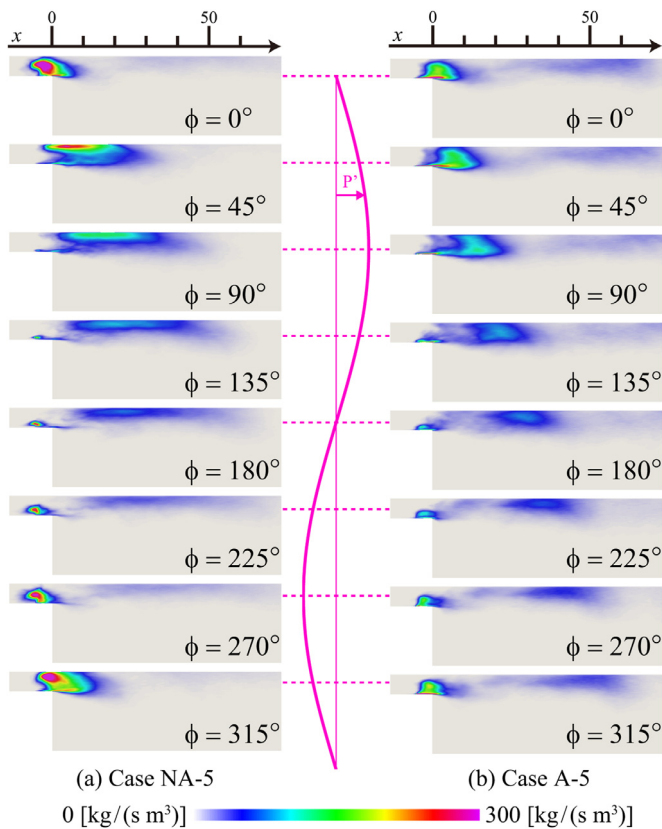
Fig. 36. Comparison of the distributions of phase- and spanwise-averaged evaporation rate, between cases without (Case NA-5) and with (Case A-5) SMD modulation.
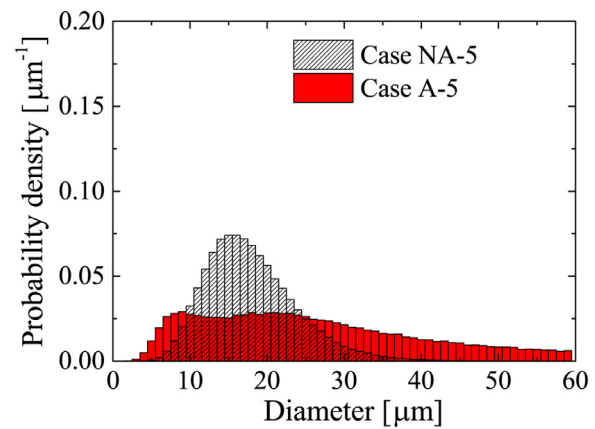

Fig. 37. Comparison of phase-averaged droplet size distributions, at the phase of $\phi = 180°$ (when $P = P_{atm}$), between cases without (Case NA-5) and with (Case A-5) SMD modulation.

Q_x in the vicinity of the dump plane is smaller in Case A-5 compared to Case NA-5. Since the distribution of heat release rate at $\phi = 90°$ is influenced by the distribution of fuel droplet evaporation rate at the previous phase, the $x - y$ planar distributions of the phase- and spanwise-averaged (z-direction) fuel droplet evaporation rate $\dot{m}_x$ at various phases of Case NA-5 and Case A-5 are shown in Fig. 36. The figure shows that the evaporation rate in the vicinity of the combustor's dump plane is smaller for Case A-5 in comparison with Case NA-5 during $\phi = 270° - 0°$. Therefore, the decrease in the heat release rate at $\phi = 90°$ is caused by the decrease in the evaporation rate during $\phi = 270° - 0°$.

Upon examining the behavior of fuel droplets after being injected in both the cases, using their post-processed LES data, it was observed that many of the droplets in the region wherein the evaporation rate was lower for Case A-5 in comparison with Case NA-5 during $\phi = 270° - 0°$, were injected at $\phi \approx 180°$ when the fuel mass flow rate is maximum (which can be confirmed from Figs. 26(d) and 17(d)). Fuel injection starts around $\phi = 90°$ and ends at $\phi = 270°$, with the peak fuel mass flow rate occurring at $\phi \approx 180°$ in Cases NA-5 and A-5 (see Figs. 17(d) and 26(d)). The SMD of injected fuel spray in Case A-5 increases rapidly during $\phi = 90° - 180°$, and attains maxima around phase $\phi = 180°$, as apparent from Fig. 26(d). Therefore, the injected fuel spray in Case A-5 is mostly comprised of large diameter fuel droplets compared to Case NA-5 in which the injected fuel spray's SMD (or droplet size distribution) is constant in time (SMD = 22.5 μm). For Case NA-5, droplet relaxation time is in the range of $\tau_d = 5.6 \times 10^{-8} - 8.34 \times 10^{-4}$ s, and turbulent time scale $\tau_t = 5.18 \times 10^{-3}$ s, hence St = $1.08 \times 10^{-5} - 0.161$. Similarly, for Case A-5, $\tau_d = 5.53 \times 10^{-8} - 8.5 \times 10^{-4}$ s and $\tau_t = 7.44 \times 10^{-3}$ s, which means St = $7.44 \times 10^{-6} - 0.114$. Additionally, due to the application of phase shift $\phi_{ph} = 270°$ in Cases NA-5 and A-5, the phase relation-

ship between the fluctuations of incoming air's streamwise velocity $\tilde{u}$ and fuel flow rate is altered (Figs. 17(d) and 26(d)), and most of the fuel droplets injected during $\phi = 90° - 270°$ reside near the dump plane, as indicated by the distributions of evaporation rate in Fig. 36. Moreover, in both Case NA-5 and Case A-5, the air mass flow rates are the same and the overall equivalence ratio is maintained at 1.0. So once again, following the same reasoning applied to Cases NA-4 and A-4 using the aforementioned details, the total droplet surface area of the injected fuel spray available for evaporation should be smaller in Case A-5 compared to Case NA-5, since it is inversely proportional to the SMD. Hence, the evaporation rate near the dump plane becomes smaller for Case A-5 compared to Case NA-5 during the subsequent phases, i.e., $\phi = 270° - 0°$.

To get an idea of the droplet sizes encountered in Cases NA-5 and A-5, the phase-averaged droplet size distributions of the fuel sprays calculated at $\phi = 180°$ (maximum fuel injection rate) are shown in Fig. 37. Similar to Cases NA-4 and A-4, the phase-averaged droplet size distribution PDFs in Fig. 37 have been computed using all the droplets within the control volume ranging from the injection ports' position to the dump plane. As mentioned before, the application of the phase shift $\phi_{ph} = 270°$ using the VMFR model to Cases NA-5 and A-5, will result in many of the fuel droplets injected during $\phi = 90° - 180°$ to still reside within this control volume at the phase $\phi = 180°$, and they are also included in the droplet size distribution PDFs in Fig. 37. The figure indicates that the droplet diameter distribution at $\phi = 180°$ becomes much wider for Case A-5, implying that its corresponding SMD also becomes larger. Since this droplet size distribution of fuel spray will influence the evaporation rate near the dump plane, Case A-5 has lower evaporation rate compared to Case NA-5. These results reveal that the reason for the pressure oscillations' RMS value becoming smaller for Case A-5 in comparison with Case NA-5, is the same as that for Cases A-4 and NA-4 discussed above.

The droplet size distribution PDF of Case A-5 in Fig. 37 is much wider or flatter than that of Case A-4 in Fig. 34. In Case A-5 the injected fuel spray consists mostly of large droplets owing to the generally large SMD values during the fuel injection period (see Fig. 26(d)). But, these injected droplets will simultaneously undergo evaporation as well and reduce in diameter during $\phi = 90° - 180°$. Therefore, when this cluster of fuel droplets is used to calculate the size distribution PDF at phase $\phi = 180°$, a flatter PDF shape is obtained for Case A-5 due to some of the previously injected (during $\phi = 90° - 180°$) large droplets having already evaporated to some extent and reduced in size. This is made possible by the longer residence time of fuel droplets in Case A-5 compared to that in Case A-4 within the above-mentioned control volume,

as a consequence of the larger value of phase shift $\phi_{ph} = 270°$ applied in Case A-5. The residence time of fuel droplets will be longer in Case A-5 compared to that in Case A-4, because the peak fuel injection rate in Case A-5 occurs around the phase when the incoming air's streamwise velocity is minimum (see Fig. 26(d)). Such tendency is not observed in the droplet size distribution PDF of Case NA-5 (even though droplet evaporation is active during the residence period), since the Lee model (SMD modulation) is not applied and the fuel droplets are injected with a size distribution PDF that remains fixed in time (corresponding to a constant SMD of 22.5 μm). The above results reveal that the effect of temporal variations in the droplet diameter distribution of liquid fuel on the intensity of combustion instability, becomes more significant as the phase shift ϕ_{ph} between the fuel flow rate fluctuations and the pressure oscillations increases. This happens because the droplet diameter distribution of the injected fuel spray becomes wider as the phase shift ϕ_{ph} increases, which enhances the strength of its effect on suppressing the increase in local evaporation rate and the accompanying increase in heat release rate, owing to the time variations of liquid fuel flow rate as discussed in Section 3.2.

4. Conclusions

In this study, LES was applied to the turbulent spray combustion field inside a back-step flow combustor to investigate the effects of temporal fluctuations in droplet diameter distribution and the flow rate of liquid fuel entering the combustor, on the spray combustion instability characteristics. For the LESs performed in this study, the average Reynolds number at the inlet of the combustor was kept constant at 4000, the initial pressure inside the combustor was 0.1 MPa, the length of the combustor was 290 mm, the overall equivalence ratio was 1.0, and the average fuel droplet diameter for the cases without SMD modulation (i.e., without Lee model) was kept constant at 18 μm (SMD = 22.5 μm). A total of 10 cases were setup and investigated in a systematic manner, by changing the conditions in the models to take into consideration the influences of fuel spray atomization (Lee model), and fuel flow rate fluctuations along with its phase difference ϕ_{ph} with the pressure oscillations (VMFR model). The following conclusions were drawn from this study:

(1) Cases NA-1 and A-1 are first considered to investigate the influence of temporal fluctuations in droplet size distribution of injected fuel spray alone, on combustion instability. With the application of the Lee model in Case A-1, the droplet diameter distribution of liquid fuel entering the combustor varies in time, depending on the fluctuations in incoming oxidizing air velocity caused by combustion instability. Moreover, this temporal fluctuation in the droplet diameter distribution tends to lower the intensity of combustion instability. The reason for this is a weakening of the correlation between heat release rate fluctuations and pressure oscillations. This results from the reduction in heat release rate near the dump plane of the combustor, caused by the broadening of droplet size distribution of liquid fuel (in Case A-1) due to the temporal fluctuations in the SMD (considered via. the Lee/atomization model). Consequently, larger diameter fuel droplets are injected which leads to a localized reduction in the evaporation rate.

(2) For the cases in which only the VMFR model is applied, but not the Lee model (i.e., Cases NA-2 to NA-5), the temporal fluctuations in the flow rate of liquid fuel injected into the combustor strongly influence the combustion instability intensity. Moreover, the combustion instability intensity increases with increasing phase shift ϕ_{ph} between the fuel flow rate fluctuations and pressure oscillations. The reason

for this is the strengthening of the correlation between the heat release rate fluctuations and the pressure oscillations. As the phase shift ϕ_{ph} increases, the heat release rate near the dump plane also increases as a consequence of increased fuel droplet residence time, and the subsequent localized increase in fuel droplet evaporation rate.

(3) For the cases in which both the VMFR model and the Lee model are applied simultaneously (i.e., Cases A-2 to A-5), the effect of temporal fluctuations in the liquid fuel droplet diameter distribution on reducing the combustion instability intensity, becomes more significant with increasing phase shift ϕ_{ph} between the liquid fuel flow rate fluctuations and the pressure oscillations. This is caused by a localized reduction in the fuel droplet evaporation rate (even though the fuel droplet residence time increases with increase in ϕ_{ph} as mentioned above), as a result of the widening in the droplet diameter distribution of the injected fuel spray (increased SMD and hence injection of larger diameter droplets) with increasing phase difference ϕ_{ph}. Hence, a localized decrease in the heat release rate is observed near the dump plane, which leads to the weakening of the correlation between heat release rate fluctuations and pressure oscillations.

The results in this study, were obtained using LES under limited conditions (mentioned above), and it is likely that the combustion instability behavior will change upon varying said conditions. This warrants further studies in the future, to investigate the effects of varying those conditions on the spray combustion instability characteristics.

Declaration of Competing Interest

The authors declare that they have no known competing financial interests or personal relationships that could have appeared to influence the work reported in this paper.

Acknowledgments

References

[1] International civil aviation organization, 2017, URL http://www.icao.int/Pages/default.aspx
[2] Japan aerospace exploration agency, 2003 URL http://www.jaxa.jp/article/special/aviation
[3] T. Lieuwen, K. McManus, Introduction: combustion dynamics in lean-premixed prevaporized (LPP) gas turbines, J. Propuls. Power 19 (5) (2003) 721.
[4] A.P. Dowling, S.R. Stow, Acoustic analysis of gas turbine combustors, J. Propuls. Power 19 (2003) 751–764.
[5] T. Lieuwen, V. Yang, Combustion instabilities in gas turbine engines: operational experience, fundamental mechanisms, and modeling, Prog. Astronaut. Aeronaut. 210 (2005) 3–26.
[6] L. Rayleigh, The explanation of certain acoustical phenomena, Nature 18 (1878) 319–321.
[7] F. Culick, M.V. Heitor, J.H. Whitelaw, Unsteady combustion, Springer Science & Business Media, 1996.
[8] M. Zhu, A.P. Dowling, K.N.C. Bray, Self-excited oscillations in combustors with spray atomizers, J. Eng. Gas Turbines Power 123 (4) (2001) 779–786.
[9] J.-Y. Lee, E. Lubarsky, B.T. Zinn, Slow active control of combustion instabilities by modification of liquid fuel spray properties, Proc. Combust. Inst. 30 (2) (2005) 1757–1764.
[10] M. de la Cruz García, E. Mastorakos, A.P. Dowling, Investigations on the self--excited oscillations in a kerosene spray flame, Combust. Flame 156 (2) (2009) 374–384.

[11] S. Tachibana, K. Saito, T. Yamamoto, M. Makida, T. Kitano, R. Kurose, Experimental and numerical investigation of thermo-acoustic instability in a liquid–fuel aero-engine combustor at elevated pressure: validity of large-eddy simulation of spray combustion, Combust. Flame 162 (6) (2015) 2621–2637.

[12] T. Kitano, K. Kaneko, R. Kurose, S. Komori, Large-eddy simulations of gas- and liquid-fueled combustion instabilities in back-step flows, Combust. Flame 170 (2016) 63–78.

[13] K. Sato, E. Knudsen, H. Pitsch, Study of combustion instabilities imposed by inlet velocity disturbance in combustor using les, ASME Turbo Expo 2009: Power for Land, Sea, and Air, American Society of Mechanical Engineers (ASME) (2009), pp. 87–99.

[14] P. Wolf, G. Staffelbach, L.Y.M. Gicquel, J.-D. Muller, T. Poinsot, Acoustic and large eddy simulation studies of azimuthal modes in annular combustion chambers, Combust. Flame 159 (11) (2012) 3398–3413.

[15] B. Franzelli, E. Riber, L.Y.M. Gicquel, T. Poinsot, Large eddy simulation of combustion instabilities in a lean partially premixed swirled flame, Combust. Flame 159 (2) (2012) 621–637.

[16] P. Moin, K.D. Squires, W.H. Cabot, S. Lee, A dynamic subgrid-scale model for compressible turbulence and scalar transport, Phys. Fluids 3 (1991) 2746–2757.

[17] C.D. Pierce, P. Moin, A dynamic model for subgrid-scale variance and dissipation rate of a conserved scalar, Phys. Fluids 10 (12) (1998) 3041–3044.

[18] J.-P. Legier, T. Poinsot, D. Veynante, Dynamically thickened flame LES model for premixed and non-premixed turbulent combustion, Summer program 2000, CTR, Stanford University (2000), pp. 157–168.

[19] F. Charlette, C. Meneveau, D. Veynante, A power-law flame wrinkling model for LES of premixed turbulent combustion part I: non-dynamic formulation and initial tests, Combust. Flame 131 (1–2) (2002) 159–180.

[20] P.A. Strakey, G. Eggenspieler, Development and validation of a thickened flame modeling approach for large eddy simulation of premixed combustion, J. Eng. Gas Turbines Power 132 (7) (2010) 071501.

[21] F. Proch, A.M. Kempf, Numerical analysis of the Cambridge stratified flame series using artificial thickened flame LES with tabulated premixed flame chemistry, Combust. Flame 161 (10) (2014) 2627–2646.

[22] A. Rittler, F. Proch, A.M. Kempf, LES of the Sydney piloted spray flame series with the PFGM/ATF approach and different sub-filter models, Combust. Flame 162 (4) (2015) 1575–1598.

[23] M. Nakamura, F. Akamatsu, R. Kurose, M. Katsuki, Combustion mechanism of liquid fuel spray in a gaseous flame, Phys. Fluids 17 (12) (2005) 123301.

[24] A.L. Pillai, R. Kurose, Combustion noise analysis of a turbulent spray flame using a hybrid DNS/APE-RF approach, Combust. Flame 200 (2019) 168–191.

[25] J. Bellan, M. Summerfield, Theoretical examination of assumptions commonly used for the gas phase surrounding a burning droplet, Combust. Flame 33 (1978) 107–122.

[26] J. Bellan, K. Harstad, Analysis of the convective evaporation of nondilute clusters of drops, Int. J. Heat Mass Transf. 30 (1) (1987) 125–136.

[27] R.S. Miller, K. Harstad, J. Bellan, Evaluation of equilibrium and non-equilibrium evaporation models for many-droplet gas-liquid flow simulations, Int. J. Multiph. Flow 24 (6) (1998) 1025–1055.

[28] C.T. Crowe, M.P. Sharma, D.E. Stock, The Particle-Source-In Cell (PSI-CELL) model for gas-droplet flows, J. Fluids Eng. 99 (2) (1977) 325–332.

[29] T. Kitano, J. Nishio, R. Kurose, S. Komori, Effects of ambient pressure, gas temperature and combustion reaction on droplet evaporation, Combust. Flame 161 (2) (2014) 551–564.

[30] B. Franzelli, E. Riber, M. Sanjosé, T. Poinsot, A two-step chemical scheme for kerosene–air premixed flames, Combust. Flame 157 (7) (2010) 1364–1373.

[31] Y. Haruki, A.L. Pillai, T. Kitano, R. Kurose, Numerical investigation of flame propagation in fuel droplet arrays, Atom. Sprays 28 (4) (2018) 357–388.

[32] T. Hara, M. Muto, T. Kitano, R. Kurose, S. Komori, Direct numerical simulation of a pulverized coal jet flame employing a global volatile matter reaction scheme based on detailed reaction mechanism, Combust. Flame 162 (2015) 4391–4407.

[33] T.-W. Lee, J.E. Park, R. Kurose, Determination of the drop size during atomization of liquid jets in cross flows, Atom. Sprays 28 (3) (2018) 241–254.

[34] A.F. Ghoniem, S. Park, A. Wachsman, A. Annaswamy, D. Wee, H.M. Altay, Mechanism of combustion dynamics in a backward-facing step stabilized premixed flame, Proc. Combust. Inst. 30 (2) (2005) 1783–1790.

[35] K.R. Mcmanus, J.C. Magill, M.F. Miller, Combustion instability suppression in liquid-fueled combustors, AIAA Paper AIAA-98-0642, 1998(1998).

[36] S. Murugappan, E.J. Gutmark, S. Acharya, M. Krstic, Extremum-seeking adaptive controller for swirl-stabilized spray combustion, Proc. Combust. Inst. 28 (2000) 731–737.

[37] K. Yu, K.J. Wilson, T.P. Parr, K.C. Schadow, An experimental study on actively controlled dump combustors, RTO AVT Symposium on "Active Control Technology for Enhanced Performance Operational Capabilities of Military Aircraft, Land Vehicles and Sea Vehicles", Braunschweig, Germany, 2000.

[38] D.A. Smith, E.E. Zukoski, Combustion instability sustained by unsteady vortex combustion, AIAA Paper 85, (1985) 1248, https://apps.dtic.mil/sti/citations/ADP011178.

[39] P. González-Tello, F. Camacho, J. Vicaria, P.A. González, A modified Nukiyama–Tanasawa distribution function and a Rosin-Rammler model for the particle–size-distribution analysis, Powder Technol. 186 (2008) 278–281.

[40] H. Moriai, R. Kurose, H. Watanabe, Y. Yano, F. Akamatsu, S. Komori, Large-eddy simulation of turbulent spray combustion in a subscale aircraft jet engine combustor–predictions of NO and soot concentrations, J. Eng. Gas Turbines Power 135 (9) (2013) 091503.

[41] R.N. Roy, M. Muto, R. Kurose, Direct numerical simulation of ignition of syngas (H$_2$/CO) mixtures with temperature and composition stratifications relevant to HCCI conditions, Int. J. Hydrogen Energy 42 (41) (2017) 26152–26161.

[42] A.L. Pillai, R. Kurose, Numerical investigation of combustion noise in an open turbulent spray flame, Appl. Acoust. 133 (2018) 16–27.

[43] Y. Hu, R. Kurose, Nonpremixed and premixed flamelets LES of partially premixed spray flames using a two-phase transport equation of progress variable, Combust. Flame 188 (2018) 227–242.

[44] Y. Hu, R. Kurose, Partially premixed flamelet in les of acetone spray flames, Proc. Combust. Inst. 37 (3) (2019) 3327–3334.

[45] Y. Hu, R. Kurose, Large-eddy simulation of turbulent autoigniting hydrogen lifted jet flame with a multi-regime flamelet approach, Int. J. Hydrogen Energy 44 (12) (2019) 6313–6324.

[46] C.T. d'Auzay, U. Ahmed, A.L. Pillai, N. Chakraborty, R. Kurose, Statistics of progress variable and mixture fraction gradients in an open turbulent jet spray flame, Fuel 247 (2019) 198–208.

[47] U. Ahmed, C.T. d'Auzay, M. Muto, N. Chakraborty, R. Kurose, Statistics of reaction progress variable and mixture fraction gradients of a pulverised coal jet flame using Direct Numerical Simulation data, Proc. Combust. Inst. 37 (3) (2019) 2821–2830.

[48] V. Moureau, C. Bérat, H. Pitsch, An efficient semi-implicit compressible solver for large-eddy simulations, J. Comput. Phys. 226 (2) (2007) 1256–1270.

[49] G.-S. Jiang, C.-W. Shu, Efficient implementation of weighted ENO schemes, J. Comput. Phys. 126 (1996) 202–228.

[50] R.J. Kee, D.-L. Graham, J. Warnatz, M.E. Coltrin, J.A. Miller, A Fortran computer code package for the evaluation of gas-phase, multicomponent transport properties, SANDIA Report No. SAND86-8246, Sandia National Laboratories, Albuquerque NM, Livermore CA, 1986.

[51] R.J. Kee, F.M. Rupley, J.A. Miller, Chemkin-II: a FORTRAN chemical kinetics package for the analysis of gas-phase chemical kinetics, SANDIA Report No. SAND89-8009B, Sandia National Laboratories, Albuquerque NM, Livermore CA, 1989.

[52] R. kurose, 2019, URL http://www.tse.me.kyoto-u.ac.jp/members/kurose/link_e.php